https://doi.org/10.5194/egusphere-2026-371
Preprint. Discussion started: 10 February 2026

Interactive Simulation of Methane and Hydrogen Soil Deposition in ECHAM5/MESSy Atmospheric Chemistry Model (EMAC) v2.55 with the new Submodel BIODEP (v1.0)

Anna Martin[1], Klaus Klingmüller[1], Benedikt Steil[1], Sergey Gromov[1], Yu-Ri Lee[2], Dong Yeong Chang[2], Nic Surawski[4], Jos Lelieveld[1,5], Sujong Jeong[3], and Andrea Pozzer[1,5]

[1]Max Planck Institute for Chemistry, Atmospheric Chemistry Department, 55128 Mainz, Germany
[2]Environmental Planning Institute, Seoul National University, Seoul, 08826, Republic of Korea
[3]Department of Environmental Management, Graduate School of Environmental Studies, Seoul National University, Seoul, 08826, Republic of Korea
[4]Centre for Green Technology, University of Technology Sydney, Gadigal Country, Ultimo NSW 2007, Australia
[5]The Cyprus Institute, Climate and Atmosphere Research Center, Nicosia, 1645, Cyprus

Correspondence: (a.martin@mpic.de)

Abstract. Methane (CH_4) and hydrogen (H_2) play critical roles in atmospheric chemistry and climate processes. CH_4 is a powerful greenhouse gas, whereas H_2, although not a greenhouse gas itself, indirectly affects radiative forcing by modifying the atmosphere's oxidative capacity and therefore the concentrations of CH_4, ozone (O_3) and stratospheric water vapor. Hydrogen is predominantly removed through microbial uptake in soils, while approximately 6% of CH_4 is taken up by soils, a factor that contributes significantly to its overall atmospheric budget. Soil uptake depends on various soil characteristics, including type, temperature, moisture, and for CH_4, nitrogen deposition. Accurately representing these influences requires a detailed understanding of both atmospheric conditions and land surface and hydrological properties. However, many Earth system models currently use fixed soil deposition rates for H_2 and CH_4, without accounting for variations in soil properties. We present BIODEP, a new biogenic deposition submodel that has been integrated into the ECHAM/MESSy Atmospheric Chemistry model (EMAC). BIODEP dynamically simulates the uptake of CH_4 and H_2 by soil, based on local meteorological and soil conditions. With BIODEP, the soil sinks of CH_4 and H_2 are updated online based on the meteorological conditions, atmospheric composition and land surface properties provided by the EMAC model. The EMAC model is coupled to the JSBACH land surface and vegetation model. This allows for a consistent and interactive treatment of soil sinks within the atmospheric chemistry model. Modeled global mean soil uptakes of 62.7 ± 11.7 Tg yr^{-1} for H_2 and 30.2 ± 4.8 Tg yr^{-1} for CH_4 are consistent with previous studies, and the resulting atmospheric mixing ratios show good agreement with observations from the NOAA GML Carbon Cycle Cooperative Global Air Sampling Network, evaluated over the period 2009–2019. In addition, comparison with column-averaged CH_4 (XCH_4) observations from the Greenhouse Gases Observing Satellite (GOSAT) demonstrates that EMAC reproduces the global and zonal-scale methane distribution with small mean biases, providing independent support for the accuracy of the simulated soil methane sink. This development makes EMAC a state-of-the-art model to interactively simulate atmospheric chemistry, including both the soil sinks of CH_4 and H_2. This enables more consistent simulation of trace

https://doi.org/10.5194/egusphere-2026-371
Preprint. Discussion started: 10 February 2026

gas budgets and an improved assessment of the feedbacks between land surface processes, atmospheric composition and future climate and emission scenarios.

1 Introduction

Methane (CH_4) is a highly potent greenhouse gas with a large climate warming potential through radiative forcing and an average atmospheric lifetime of approximately 9–12 years (IPCC, 2023). Approximately 6% of the atmospheric CH_4 is removed via soil uptake by methanotrophic bacteria particularly in well-aerated upland soils (Saunois et al., 2025). This sink is sensitive to environmental conditions, especially soil temperature, moisture, and nitrogen availability (Murguia-Flores et al., 2018; Singh et al., 1997; Van den Pol-van Dasselaar et al., 1998; Wang et al., 2005). Numerous studies have quantified CH_4 uptake across various ecosystems and climatic regions (Dutaur and Verchot, 2007; Shushi et al., 2020; Saunois et al., 2016; Ito and Inatomi, 2012; Kleinen et al., 2020; Murguia-Flores et al., 2018). Table 1 summarizes CH_4 soil uptake rates reported in selected studies as described in the recent methane budget review by Saunois et al. (2019). Estimated uptake values range from $18\ \mathrm{Tg\ CH_4\ yr^{-1}}$, as reported by Kleinen et al. (2020), to $39.5\ \mathrm{Tg\ CH_4\ yr^{-1}}$ according to Murguia-Flores et al. (2018). As these fluxes are strongly affected by climate change, understanding the behavior of the soil CH_4 sink under future conditions is crucial for reliable projections of atmospheric methane levels.

Hydrogen (H_2) has the potential to be used as clean energy carrier, especially for hard-to-electrify sectors (Schultz et al., 2003; Tromp et al., 2003; Hauglustaine et al., 2022). However, the transition to a hydrogen-based energy system introduces new uncertainties related to atmospheric chemistry. Although H_2 itself is not a greenhouse gas, it indirectly influences climate by reacting with hydroxyl radicals (OH), thereby reducing the oxidative capacity of the atmosphere and prolonging the lifetime of CH_4 and other pollutants (Ehhalt and Rohrer, 2009; Sand et al., 2023). The major source of H_2 is photochemical oxidation of CH_4 and non methane VOCs, accounting for 54.94% of the total H_2 emissions (Ouyang et al., 2025). CH_4 alone contributes 26.6% to the total H_2 source (Derwent and Jenkin, 2024). Therefore H_2 is strongly connected to the CH_4 budget. Under current conditions, the global hydrogen budget is approximately balanced, with the dominant removal process being soil uptake—accounting for 70–80 % of total H_2 loss (Constant et al., 2009; Ehhalt and Rohrer, 2009; Paulot et al., 2024). This soil sink is driven by similar environmental variables as the CH_4 sink, making it particularly sensitive to climate variability. Increases in H_2 emissions, particularly through leakage in future hydrogen usage scenarios, could disturb this balance, potentially enhancing climate forcing via secondary effects on methane, ozone, and stratospheric water vapor (Trapani et al., 2025; Sand et al., 2023). Recent studies have quantified the indirect warming potential of H_2 using the Global Warming Potential over 100 years (GWP_{100}) metric. Sand et al. (2023) estimate a model-mean GWP_{100} for H_2 of 11.6 ± 2.8, with the largest contribution arising from enhanced CH_4 due to OH removal. However, they also highlight that the dominant uncertainty in this estimate stems from the poorly constrained soil sink of H_2, motivating the need for improved process-based modeling.

Since CH_4 and H_2 sink processes are closely linked to meteorological conditions, the state of the climate and chemical interactions, such as the reactivity of OH, it is essential to accurately represent these coupled processes for reliable climate impact assessments.

https://doi.org/10.5194/egusphere-2026-371
Preprint. Discussion started: 10 February 2026

To address this, we present and evaluate a new BIOgenic DEPosition submodel BIODEP, which dynamically calculates the soil sink fluxes of both CH_4 and H_2 based on local soil and meteorological conditions. BIODEP is implemented within the EMAC (ECHAM/MESSy Atmospheric Chemistry) model. While BIODEP adopts the same soil sink parametrization for microbial uptake in aerobic soils as presented by Surawski et al. (2025), it replaces the externally prescribed ERA5 soil moisture and temperature reanalysis with interactive data from the coupled EMAC/JSBACH model. This dynamic coupling enables the online calculation of H_2 soil deposition fluxes within EMAC, allowing atmospheric H_2 dynamics to be consistently updated in response to evolving land-surface conditions. For CH_4, the sink parametrization is based on the approach of Murguia-Flores et al. (2018), incorporating dependencies on the online interactively calculated soil temperature, moisture, and nitrogen deposition. The CH_4 soil uptake fluxes are interactively calculated and coupled to EMAC's tracer budget, allowing for real-time updates of atmospheric CH_4 tendencies. This study presents the evaluation of BIODEP under present-day conditions. We assess the simulated soil uptake fluxes against available observational constraints and benchmark the model performance for both CH_4 and H_2 data. By providing a dynamic and coupled treatment of these important trace gas sinks, BIODEP enhances EMAC's capacity to simulate future scenarios involving hydrogen deployment and climate-driven changes in the soil environment.

Table 1. Global soil CH_4 uptake estimates from the literature

Reference	**Time-frame**	**Description**	**Global soil CH_4 uptake (Tg CH_4 yr^{-1})**
Measurement studies			
Dutaur and Verchot (2007)	–	–	36 ± 23
Combined Measurement and Model dataset			
Shushi et al. (2020)	2010–2018	Soil CH_4 fluxes observed at 682 sites combined with a machine-learning algorithm for a data-driven estimate of monthly global soil CH_4 uptake	28.65 ± 6.1
Model studies			
Saunois et al. (2016)	–	Ridgwell et al. (1999) parametrization improved by Curry (2007)	28 range: 9–4
Ito and Inatomi (2012)	–	Ensemble	25–35
Kleinen et al. (2020)	2000–2020	JSBACH model	18
Ito and Inatomi (2012)	2000–2020	VISIT model	35
Murguia-Flores et al. (2018)	1990–2009	MeMo model	37.5
		Ridgwell et al. (1999) parametrization	39.5
		Curry (2007) parametrization	31.3
This work	2009–2019	EMAC coupled to JSBACH and BIODEP	30.2 ± 4.8

https://doi.org/10.5194/egusphere-2026-371
Preprint. Discussion started: 10 February 2026

2 Evaluation datasets

We evaluate the performance of the BIODEP submodel by comparing simulated atmospheric mixing ratios of hydrogen (H_2) and methane (CH_4) against observational datasets for the period 2009–2019. For hydrogen, simulated H_2 concentrations (in ppbv) from BIODEP are compared to observations from the NOAA GML Carbon Cycle Cooperative Global Air Sampling Network, which provides data from 51 global stations (Pétron et al., 2024). For methane, simulated CH_4 mixing ratios (in ppbv) are evaluated against observations from the NOAA GML network (Lan et al., 2025), covering a global set of monitoring sites with available data between 2009 and 2019. Quality control procedures and the impact of the COVID-19 pandemic result in data gaps or missing data at some stations. These comparisons allow us to assess the model's ability to reproduce atmospheric concentration levels and spatial patterns of both trace gases. In addition to surface mixing ratios, column-averaged dry-air mole fractions of methane (XCH_4) are compared with the bias-corrected monthly GOSAT (Greenhouse gases Observing SATellite) product (Version 03.05) (NIES, 2024). GOSAT, the world's first satellite dedicated to monitoring the greenhouse gases of carbon dioxide and methane, was launched in January 2009 by the Japan Aerospace Exploration Agency (JAXA) (Kuze et al., 2009). The Thermal And Near infrared Sensor for carbon Observation Fourier-Transform Spectrometer (TANSO-FTS) instrument onboard GOSAT measures shortwave infrared spectra to retrieve XCH_4 (Kuze et al., 2009; Parker et al., 2020). The GOSAT methane product is widely recognized for its high quality and long-term record (Jacob et al., 2022).

3 Model description and setup

3.0.1 EMAC

The ECHAM/MESSy Atmospheric Chemistry (EMAC) model is a numerical chemistry and climate simulation system that includes sub-models describing tropospheric and middle atmosphere processes and their interaction with oceans, land and human influences (Jöckel et al., 2010). It uses the second version of the Modular Earth Submodel System (MESSy2) to link multi-institutional computer codes. The core atmospheric model is the fifth-generation European Center Hamburg general circulation model (ECHAM5, (Roeckner et al., 2006)). The physics subroutines of the original ECHAM code have been modularized and re-implemented as MESSy submodels and have continuously been further developed. Only the spectral transform core, the flux-form semi-Lagrangian large-scale advection scheme, and the nudging routines for Newtonian relaxation remain from ECHAM. Further details on EMAC are documented by (Jöckel et al., 2016) and can be found on the MESSy website[1]. In this study, we utilized EMAC (MESSy version 2.55.0) at a resolution of T63L31ECMWF. This configuration corresponds to a spherical truncation of T63, which translates to a quadratic Gaussian grid with approximately 1.8 by 1.8 degrees spacing in latitude and longitude, and includes 31 vertical hybrid pressure levels extending up to 10 hPa. Each simulation conducted in this study includes 11 years of simulation data from January 2009 to December 2019. Simulations are nudged towards ERA-Interim meteorological reanalysis data (Berrisford et al., 2011) from the European Center for Medium-Range Weather

[1] https://www.messy-interace.org

https://doi.org/10.5194/egusphere-2026-371
Preprint. Discussion started: 10 February 2026

Forecasts (ECMWF) (Jeuken et al., 1996; Jöckel et al., 2006). This study uses the model configuration described in (Kohl et al., 2023).

EMAC has recently been coupled to version four of the Jena Scheme for Biosphere-Atmosphere Coupling in Hamburg (JSBACH) (Martin et al., 2024). JSBACH is a comprehensive land surface and vegetation model developed to simulate a wide range of biogeochemical processes within terrestrial ecosystems (Reick et al., 2021; Schneck et al., 2022). Among other improvements, JSBACH replaces the bucket soil hydrology scheme included in the former SURFACE submodel of EMAC with a comprehensive five-layer soil hydrology model, leading to improved representation of surface energy fluxes and reduction of biases related to surface temperature and vegetation stress. This updated framework allows the investigation of biogeochemical processes at finer temporal resolutions, facilitating a more detailed understanding of land-atmosphere interactions and their impact on atmospheric chemistry. JSBACH uses a vertical structure of five snow layers, three canopy layers and five soil layers to a depth of 9.8 meters. The model includes 11 plant functional types (PFTs), including tropical and extratropical broadleaf evergreen and deciduous trees, broadleaf and deciduous shrubs, C_3 and C_4 grasses, and C_3 and C_4 pastures and crops. The JSBACH model initialization is based on carbon pools, soil properties and land characteristics of the year 2005, with system equilibration expected within approximately five years (Martin et al., 2024). While atmospheric variables typically stabilize within a few days, soil moisture adjusts more slowly, with an equilibration time of up to one year (Hagemann and Stacke, 2015; Schneck et al., 2022). The simulation setups employ the same emission inventories as Surawski et al. (2025).

CH_4 emissions correspond to the year 2020 and include twelve categories (e.g., wetlands, agriculture, fossil fuel sectors), using the emission fields of the Global Atmospheric Methane Synthesis (GAMeS) inventory (Houweling et al., 1999) and the GFEDv4s emission datasets for biomass burning (Randerson et al., 2017). In the original configuration, emissions of CH_4 were scaled according to the atmospheric OH concentration in order to reproduce observed methane levels (Zimmermann et al., 2020). Since the model setup has been updated to include an improved land surface and vegetation model, as well as interactive biogenic emissions and several changes to the chemistry setup, the formation of tropospheric ozone and, subsequent global oxidation capacity of the atmosphere driven by OH has changed. As OH is the dominant sink for methane, changes in its concentration directly affect the lifetime of methane. Consequently, the CH_4 emissions were scaled by a factor of 0.90 for emission sources and 1.06 for emissions responsible for long-term trends to align with the updated OH distribution and maintain consistency with the global mean methane observations from the from the NOAA Global Monitoring Laboratory (NOAA Global Monitoring Laboratory (GML), 2025) for the period 2009–2019. The comparison of the scaled mixing ratio of the simulation and the NOAA GML network datasets is documented in Figure A1 the Appendix. H_2 emissions are based on the RETRO dataset (year 2000) and include anthropogenic, biomass burning, soil, and oceanic sources (Schultz et al., 2008). All emissions are annually repeated, excluding inter annual variability, and optimized for steady-state simulations representative of present-day conditions.

3.1 Methane deposition parametrization

The newly implemented Soil Methanotrophy Model (MeMo v1.0) (Murguia-Flores et al., 2018) in EMAC simulates soil–atmosphere CH_4 exchange by solving a steady-state, one-dimensional diffusion–reaction equation that accounts for microbial CH_4 oxida-

https://doi.org/10.5194/egusphere-2026-371
Preprint. Discussion started: 10 February 2026

tion throughout the soil profile. CH_4 uptake is controlled by the balance between gas-phase diffusion and microbial oxidation, governed by spatially variable parameters for the CH_4 diffusion coefficient (D_{CH_4}) and first-order oxidation rate constant (k_d). Following (Murguia-Flores et al., 2018), the soil uptake flux of CH_4 (J_{CH_4}) is given as:

$$J_{CH_4} = \sqrt{k_d \, D_{CH_4}} \, (A - B) \tag{1}$$

with

$$A = -\frac{C_{CH_4} \times \exp\left(\sqrt{\frac{k_d}{D_{CH_4}}} L\right) - CH_{4\min}}{\left[\exp\left(-\sqrt{\frac{k_d}{D_{CH_4}}} L\right) - \exp\left(\sqrt{\frac{k_d}{D_{CH_4}}} L\right)\right]} \tag{2}$$

and

$$B = \frac{-CH_{4\min} + C_{CH_4} \times \exp\left(-\sqrt{\frac{k_d}{D_{CH_4}}} L\right)}{\left[\exp\left(-\sqrt{\frac{k_d}{D_{CH_4}}} L\right) - \exp\left(\sqrt{\frac{k_d}{D_{CH_4}}} L\right)\right]} \tag{3}$$

C_{CH_4} is the atmospheric CH_4 concentration (in ppbv), $CH_{4,\min}$ (in $\mathrm{mg\,m^{-3}}$) represents the threshold for the minimum CH_4 concentration within the soil. This value is set to the biological limit of 100 ppbv, and L (in cm) denotes the depth of soil for 99.9% CH_4 uptake.

3.1.1 Soil air diffusivity D_{CH_4}

The soil air diffusivity D_{CH_4} is calculated as $D_{CH_4} = D_0\,CH_4 \times G_T \times G_{\text{soil}}$, where $D_0\,CH_4 = 0.196\ \mathrm{cm^2\,s^{-1}}$ is the diffusion coefficient of methane in free air at standard temperature and pressure, G_T is the temperature response factor and G_{soil} is the dimensionless soil structure factor. The temperature response is derived from the temperature T (in °C) based on (Moldrup et al., 1996, 2013) with $G_T = 1.0 + 0.0055 \times T$. The soil structure factor G_{soil} is computed as:

$$G_{\text{soil}} = \phi^{4/3} \left(\frac{\phi_{\text{air}}}{\phi}\right)^{1.5+\frac{3}{b}}, \tag{4}$$

with $b = 15.9 \times f_{\text{clay}} + 2.91$, a scalar dependent on the clay content (f_{clay} in %), ϕ the total pore volume (in $\mathrm{cm^3\,cm^{-3}}$), based on the bulk density ρ (in $\mathrm{g\,cm^{-3}}$) and the particle density of soil $d = 2.65\,\mathrm{g\,cm^{-3}}$:

$$\phi = 1 - \left(\frac{\rho}{d}\right) \tag{5}$$

and the air-filled porosity ϕ_{air} (in $\mathrm{cm^3\,cm^{-3}}$) which is depended on the volumetric soil water content Θ (in %) :

$$\phi_{\text{air}} = \phi - \Theta. \tag{6}$$

https://doi.org/10.5194/egusphere-2026-371
Preprint. Discussion started: 10 February 2026

3.1.2 Oxidation rate constant k_d

The CH_4 oxidation rate constant k_d in MeMo is calculated as:

$$k_d = k_0 \times r_{\mathrm{SM}} \times r_T \times r_N, \tag{7}$$

with the base oxidation rate constant for uncultivated moist soil at $0\,^{\circ}\mathrm{C}$ k_0 and the scaling factors accounting for the effects of soil moisture (r_{SM}), temperature (r_T), and nitrogen content (r_N) (Murguia-Flores et al., 2018) To improve accuracy, MeMo uses biome-specific k_0 values derived from time-series data on soil CH_4 uptake, temperature, and moisture from three ecosystems: temperate forest, tropical rainforest, steppe and other (Luo et al., 2013). Those ecosystems are based on the cover fraction of individual plant functional types in JSBACH. Table 2 shows the ecosystems, the corresponding k_0 values and their associated Plant Functional Types (PFTs) based on JSBACH PFT classifications. Murguia-Flores et al. (2018) note that uncertainties regarding the k_0 value persist, particularly in tropical regions, due to limited observational data. To prevent overestimation of CH_4 fluxes, lower k_0 values are typically used in these areas.

Table 2. Ecosystem classification and corresponding base oxidation rate constant k_0 in s^{-1}, based on (Luo et al., 2013), and corresponding JSBACH plant functional types (PFTs).

Ecosystem	k_0 (s^{-1})	JSBACH PFT
Temperate forest	4.0×10^{-5}	Extra-tropical forests
Tropical forest	1.6×10^{-5}	Tropical forests
Steppe	3.6×10^{-5}	Grass
Other ecosystems	5.0×10^{-5}	Shrubs, pasture, and crops

3.1.3 Soil moisture contribution r_{SM}

In MeMo, the CH_4 oxidation rate constant k_d is scaled by soil moisture, temperature and soil nitrogen deposition. The influence of soil moisture is represented by the soil moisture factor r_{SM}, which quantifies the effect of moisture on methane uptake. Low moisture levels reduce microbial activity as water is required for microbial metabolism and gas diffusion. Conversely, too high moisture levels inhibit the diffusion of methane and oxygen into the soil, limiting microbial oxidation. This results in an optimum soil moisture content for methane uptake, where the soil moisture factor r_{SM} peaks for efficient microbial oxidation of CH_4. r_{SM} is calculated based on the volumetric soil moisture fraction SM following (Murguia-Flores et al., 2018):

$$r_{\mathrm{SM}} = \left[1 - \frac{\log_{10}(1 - SM) - \log_{10}(0.2)}{\log_{10}(100) - \log_{10}(0.2)}\right]^{0.8}, \quad \text{for } SM < 0.2 \tag{8}$$

https://doi.org/10.5194/egusphere-2026-371
Preprint. Discussion started: 10 February 2026

and

$$r_{\mathrm{SM}} = \frac{1}{\sqrt{2\pi}} \exp\left(-\frac{1}{2}\left(\frac{SM - 0.2}{0.2}\right)^2\right), \quad \text{for } SM > 0.2 \tag{9}$$

3.1.4 Soil temperature contribution r_T

The second scaling factor of the CH_4 oxidation rate constant k_d accounts for soil temperature and is referred to as r_T. This factor accounts for the influence of temperature on methane oxidation, reflecting the high sensitivity of microbial activity to temperature variations and is calculated following (Murguia-Flores et al., 2018) as:

$$r_T = \exp\left(0.1515 + 0.05238T - 5.946 \times 10^{-7} T^4\right) \quad \text{for } T > 0°\mathrm{C} \tag{10}$$

and

$$r_T = \frac{1}{\exp(-T)} \quad \text{for } T < 0°\mathrm{C} \tag{11}$$

The model predicts maximum CH_4 uptake at approximately 25 °C, where r_T reaches its peak. The temperature dependency in MeMo captures the observed exponential decline in CH_4 uptake at subzero temperatures, aligning well with field observations that show methanotrophic activity persists even below 0 °C (Murguia-Flores et al., 2018). Compared to earlier models, the r_T formulation in MeMo more accurately reflects real-world patterns of soil methane oxidation. A detailed description of the derivation of this formulation—based on the work of (Castro et al., 1995) and (Grosso et al., 2000) and its comparison to other soil methanotrophy models is provided in (Murguia-Flores et al., 2018).

3.1.5 Soil nitrogen deposition contribution r_N

The third contributing factor is the nitrogen scaling factor r_N. It accounts for the inhibitory effect of nitrogen (N) inputs from atmospheric deposition N_{dep} and fertilizer application N_{fert} (both in kg N ha^{-1} yr^{-1}) on soil CH_4 uptake. Scaled by soil bulk density ρ (in g cm^{-3}) and depth z (in cm), the total soil nitrogen deposition in soil N_{soil} (in kg N m^{-2} yr^{-1}) is as follows:

$$N_{\mathrm{soil}} = \frac{N_{\mathrm{dep}} + N_{\mathrm{fert}}}{\rho \times z} \tag{12}$$

Methanotrophic bacteria responsible for methane oxidation can be negatively affected by excess nitrogen through a number of mechanisms. These include substrate competition with ammonia-oxidizing bacteria (Gulledge and Schimel, 1998; Bradford et al., 2001; Phillips et al., 2001), toxicity from intermediates such as hydroxylamine and nitrite (Bronson and Mosier, 1994; MacDonald et al., 1996; Sitaula et al., 2000), and osmotic stress induced by high concentrations of ammonium salts (Whalen, 2000). Although some studies have reported positive effects of N inputs on CH_4 uptake, attributed to stimulated activity of nitrifying bacteria under improved nutrient conditions (Cai and Mosier, 2000; De Visscher and Van Cleemput, 2003; Rigler

https://doi.org/10.5194/egusphere-2026-371
Preprint. Discussion started: 10 February 2026

and Zechmeister-Boltenstern, 1999), observational datasets support a net inhibitory effect in most ecosystems (Aronson and Helliker, 2010; Butterbach-Bahl and Papen, 2002; Steinkamp et al., 2001). Therefore, MeMo assumes a consistent negative effect of nitrogen inputs on CH_4 uptake. Nitrogen inhibition r_N is then calculated based on the empirical inhibition coefficient $\alpha = 0.0033$ (i.e. 0.33 % reduction in CH_4 uptake per mol N added) derived from field and laboratory studies (Zhuang et al., 2013):

$$r_N = 1 - (N_{\text{soil}} \times \alpha) \tag{13}$$

MeMo optionally includes the upward CH_4 flux ($F_{CH_4} > 0$) from wetlands, permafrost, or areas with anaerobic microsites, representing methane production below the surface, as a lower boundary condition. This allows the model to simulate not only the uptake of atmospheric methane but also the consumption of internally produced methane. However, due to the lack of measurement data, this feature was not evaluated and tested in this study.

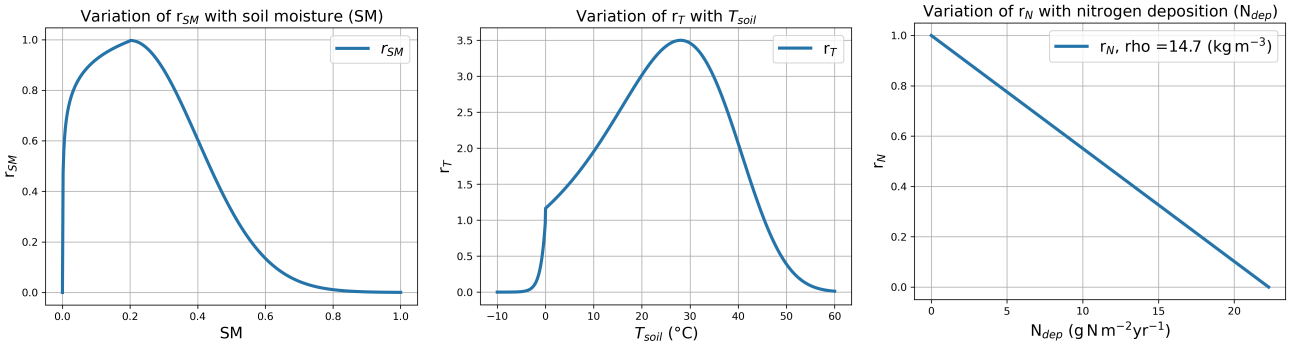

(a) (b) (c)

Figure 1. CH_4 uptake responses as a function of (a) fractional soil moisture (r_{SM} versus soil moisture, SM), (b) soil temperature (response factor r_T versus soil temperature, T_{soil}, in °C), and (c) nitrogen deposition and fertilizer application (response factor r_N versus nitrogen deposition, N_{dep}, in g N m^{-2} yr^{-1}). The factor r_N is derived using an initial bulk density of 14.7 kg m^{-3}.

3.1.6 Hydrogen deposition parametrization

The soil deposition scheme implemented in BIODEP for hydrogen is described in detail in Surawski et al. (2025), following the algorithm of Paulot et al. (2021); Ehhalt and Rohrer (2013); Yonemura et al. (2000). It estimates the rate at which molecular hydrogen is removed from the atmosphere by the soil using a two-layer soil model that accounts for physical diffusion and microbial activity. Physical diffusion is considered in the top soil layer and depends on soil water content, temperature and surface pressure. The water content and thickness of the top layer are calculated from porosity, total column water content and empirical thresholds depending on the eolian and sand and loess loam fractions (Surawski et al., 2025) while these fractions are taken from the LDAS/GLDAS data sets (Rodell et al., 2004), porosity and total water column content are derived from the optimized soil hydrology in EMAC, provided by the JSBACH submodel. Microbial activity of hydrogen-oxidizing bacteria is

https://doi.org/10.5194/egusphere-2026-371
Preprint. Discussion started: 10 February 2026

considered in the second (lower) soil layer, which also depends on soil temperature and moisture of the second soil layer. The
225 soil moisture is derived as the remaining water in the top 10 cm of the soil, derived from the JSBACH submodel. The temperature dependence is given by (Ehhalt and Rohrer, 2013). The H_2 uptake rate is then determined by the diffusion resistance of snow and the top soil layer plus the microbial uptake in layer 2. The latter is multiplied by a constant A representing bacterial activity, following Yashiro et al. (2011). This factor is used to calibrate to a global mean deposition rate over land to 0.033 cm s^{-1} (Figure 2).

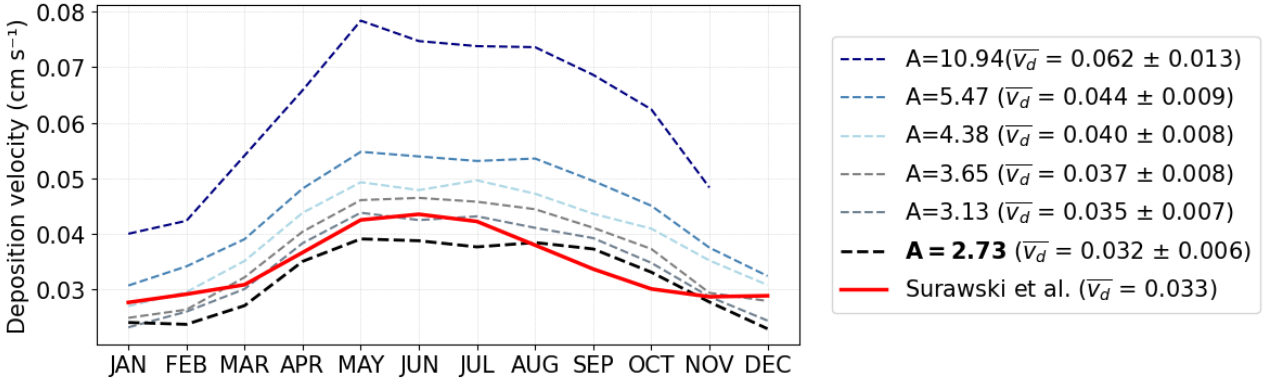

Figure 2. Monthly mean soil H_2 deposition velocities in 2009 from the BIODEP model with different tuning factors (A). The black dashed line shows the chosen factor A, matching the land average of 0.033 cm s^{-1}, while the red line shows data from Surawski et al. (2025).

https://doi.org/10.5194/egusphere-2026-371
Preprint. Discussion started: 10 February 2026

3.1.7 Driving data for methane and hydrogen deposition parameterizations

The input data required for both the H_2 and CH_4 deposition subroutines is obtained online from the EMAC model, which, thanks also to different submodels (e.g. SCAV, DRYDEP, JSBACH (Tost et al., 2006; Kerkweg et al., 2006; Martin et al., 2024)) provides all relevant atmospheric and surface variables including surface temperature (T), surface pressure, atmospheric H_2 and CH_4 concentration, nitrogen deposition (N_{dep}), soil porosity (ϕ), soil moisture (SM), soil depth (z), and ecosystem properties. In addition, soil properties such as clay fraction (f_{clay}), sand fraction (f_{sand}), and bulk density (ρ) are obtained from the global soil dataset by (Shangguan et al., 2014). Following (Murguia-Flores et al., 2018), anthropogenic nitrogen input is derived from the historical global maps of NH_4^+ and NO_3^- application in synthetic nitrogen fertilizers (N_{fert}), as provided by (Nishina et al., 2017).

4 Results and discussion

Table 3 summarizes the weighted global average values (± standard deviation) for the deposition velocity (cm s^{-1}), soil uptake (Tg yr^{-1}), and total global atmospheric burden of H_2 and CH_4 (Tg). These values are compared with observational datasets (H_2 measurements from Pétron et al. (2024), CH_4 measurements from Lan et al. (2025) and NIES (2024)), and modeled datasets by Surawski et al. (2025) (H_2 deposition velocity, uptake, and burden) and the MeMo data from 2000 (CH_4, uptake Murguia-Flores et al. (2018)). Deposition velocity's and uptake are averaged only over land. As the GOSAT dataset (NIES, 2024) is only available from starting from June 2009 the atmospheric burden of the total column (Tg) is only compared starting from June 2009 till December 2019.

Table 3. Comparison summary of model results, observational data, and reference datasets. Values represent weighted global averages ± standard deviation from the model simulations and reference data. Deposition velocities and soil uptake are averaged over land areas only.

Reference	Timeframe	Deposition velocity (cm s^{-1})	Soil Sink (Tg yr^{-1})	Atmospheric burden at surface (Tg)	Atmospheric burden total column (Tg)
CH_4					
Lan et al. (2025)	2010–2020	–	–	5300.0 ± 165.6	–
Murguia-Flores et al. (2018)	2000	–	38.0 ± 8.4	–	–
NIES (2024)	June 2009–2019	–	–	–	5108.7 ± 73.0
This work	2009–2019	0.0006 ± 0.0001	30.2 ± 4.8	5252.8 ± 86.3	5110.5 ± 74.3
H_2					
Pétron et al. (2024)	2020 (avg.)	–	–	190.9 ± 7.2	
Surawski et al. (2025)	2010–2020	0.033	60.5 ± 0.07	199.6 ± 0.2	
This work	2009–2019	0.033 ± 0.007	62.7 ± 11.7	204.9 ± 6.1	

https://doi.org/10.5194/egusphere-2026-371
Preprint. Discussion started: 10 February 2026

4.1 Comparison of methane mixing ratio against observations

Figure 3 shows the average CH_4 mixing ratio of the EMAC model together with the individual on the site-level flask observational station data from the NOAA GML network (Lan et al., 2025) averaged over the period 2009-2019. Panel (a) illustrates the spatial distribution of mean modeled CH_4 mixing ratios, while panel (b) presents the Pearson correlation coefficients (r) between EMAC-simulated and observed CH_4 values at individual monitoring stations.

A summary of the amount of available observations, mean modeled and observed CH_4 mixing ratios, and the model–observation differences is provided in Table A1 in the Appendix. The corresponding time series for each station are shown in Figures A3 of the Appendix. The CH_4 mixing ratios are well reproduced with 43 out of 51 stations showing high correlation ($r > 0.6$) between the EMAC simulations and station datasets, as shown in Figure 3a. Correlations between EMAC simulations and observational data exceeding $r > 0.90$ are found at several stations, including EIC in Chile ($r = 0.96$), HBA in Antarctica ($r = 0.95$), BHD in New Zealand ($r = 0.96$), and USH in Argentina ($r = 0.97$). These stations are predominantly situated in remote, coastal, island, or Southern Hemisphere regions, often at lower latitudes or in polar areas with low anthropogenic background emissions. EMAC captures regional-scale methane transport and background levels without being affected by local sources or sinks. In contrast, low or even negative correlations between EMAC simulations and observational CH_4 data are found at Northern Hemisphere stations (latitude > 0.55°), including ZEP in Norway ($r = 0.49$), PAL in Finland ($r = 0.05$), or AMY in South Korea ($r = -0.25$). These sites are located in regions where complex local sources and sinks including wetland emissions and seasonal soil uptake contribute significantly to methane variability, which are not fully captured at the 1.8° resolution of EMAC simulations. The meridional gradient and seasonal cycle of CH_4, as derived from both EMAC model output and observational data, are shown in Figure 4. As illustrated in Figure 4a, both datasets show a clear inter hemispheric gradient, characterized by higher CH_4 mixing ratios in the Northern Hemisphere. This distribution is primarily driven by greater anthropogenic emissions in the Northern Hemisphere, notably from fossil fuel combustion, industrial activities, and biomass burning. The EMAC simulation accurately reflects the observed meridional gradient. The seasonal cycle (Figure 4b), separated into northern and southern hemispheres, shows generally good agreement between EMAC and the observational station data. In the Northern Hemisphere, the model slightly overestimates CH_4 throughout the year, with a more pronounced overestimation in July and August. Instead of reproducing the small summertime minimum seen in the observations, the model displays a weak maximum, likely influenced by a few outlier stations. In contrast, the Southern Hemisphere seasonal cycle aligns very well with the observational data. Due to its long atmospheric lifetime (9–12 years) and relatively steady global sources, CH_4 exhibits only minor seasonal variations at the hemispheric and global scale. EMAC reproduces this small seasonal variability in agreement with the observations and generally within their standard deviations. In summary, results from the EMAC model accurately captures atmospheric methane variability at many remote stations, particularly in tropical and Southern Hemisphere regions, where the correlation between modeled and observed values is consistently high. These sites are characterized by cleaner air and low local anthropogenic and natural emissions. Conversely, model performance is weaker at stations affected by complex topography and anthropogenic or wetland emissions where low or even negative correlations suggest discrepancies in the seasonal and inter annual patterns of methane dynamics. EMAC reproduces the latitudinal gradient and seasonal

https://doi.org/10.5194/egusphere-2026-371
Preprint. Discussion started: 10 February 2026

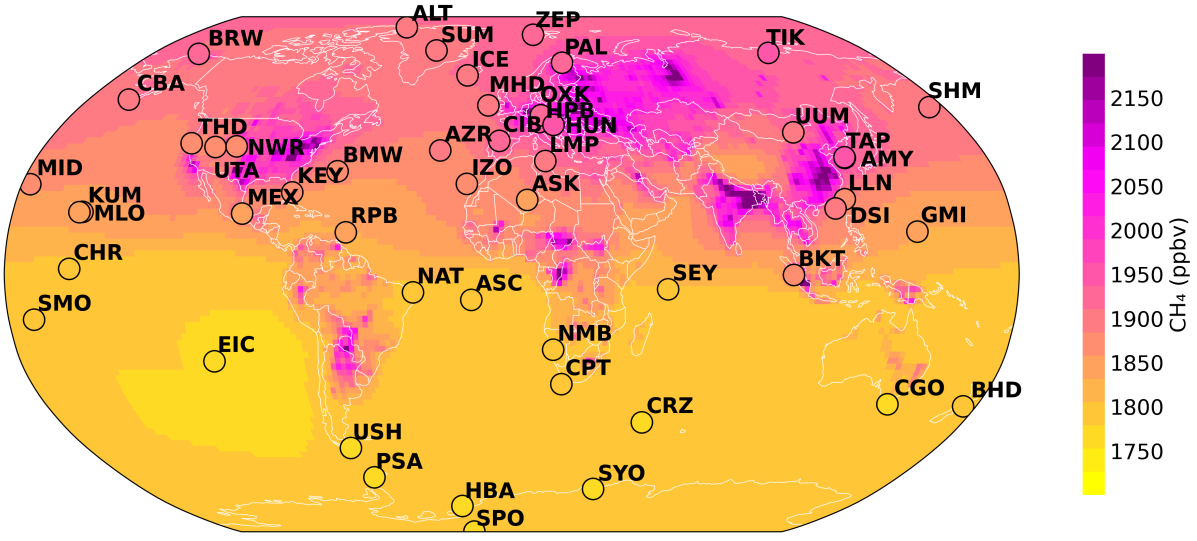

(a)

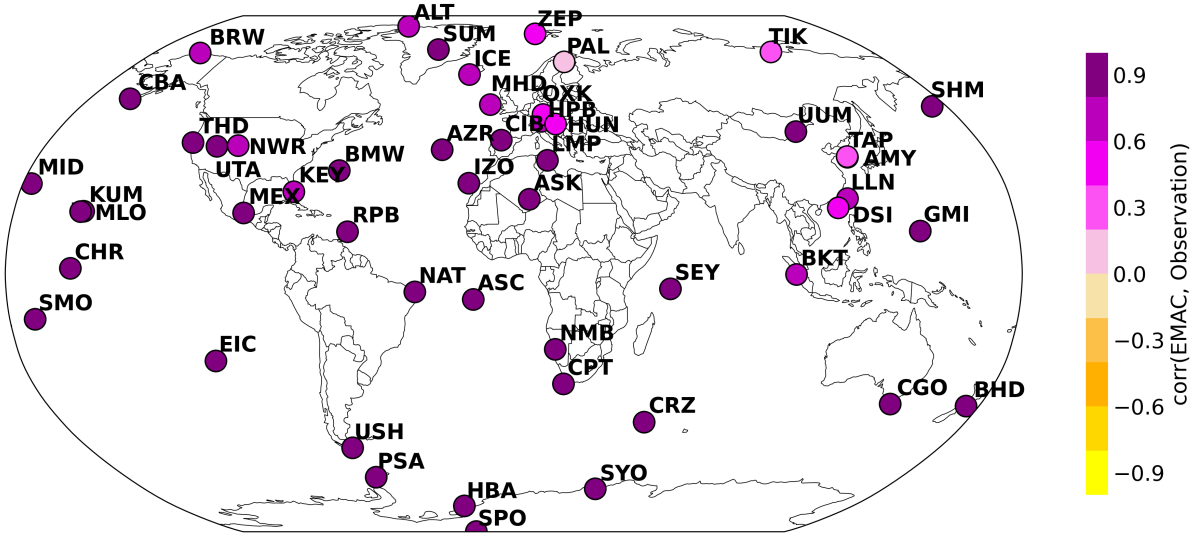

(b)

Figure 3. Comparison of modeled and observed surface CH_4 data averaged over the years 2009-2019. Circles indicate the location of the observational stations Panel (a) shows the global distribution of mean CH_4 mixing ratio (ppbv), and panel (b) shows the corresponding Pearson correlation coefficient between the observation stations and EMAC results using the BIODEP submodel.

cycle of atmospheric methane as observed in measurements. Both the model and the observations show higher methane mixing ratios in the Northern Hemisphere, driven by greater anthropogenic emissions from sources such as fossil fuel use, industry,

https://doi.org/10.5194/egusphere-2026-371
Preprint. Discussion started: 10 February 2026

and biomass burning. The model captures seasonal variability well, remaining within the range of observational uncertainty throughout the year. A global methane soil sink of 30.2 ± 4.8 Tg yr^{-1} is estimated, which is consistent with previous literature (see Table 1).

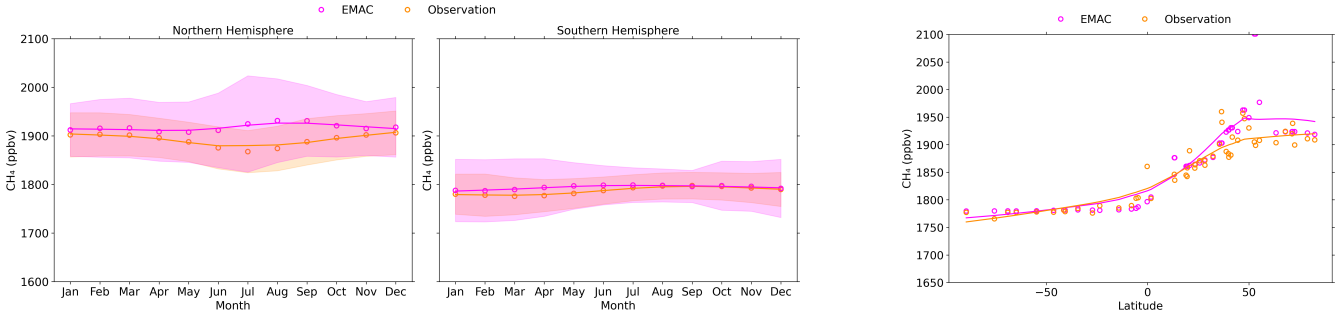

(a) (b)

Figure 4. Comparison of modeled and observed surface CH_4 data from 2009 to 2019. Solid lines represent smoothed trends obtained using locally estimated scatterplot smoothing (LOESS) with a smoothing parameter of 2/3 and locally linear fitting. Panel (a) shows the seasonal variability of modeled and observed CH_4 data. Shaded areas represent the temporal standard deviations. Panel (b) shows the meridional distribution of CH_4 based on EMAC model outputs and observational data from stations with at least 12 monthly measurements.

4.1.1 Comparison of total column CH_4 against satellite measurements

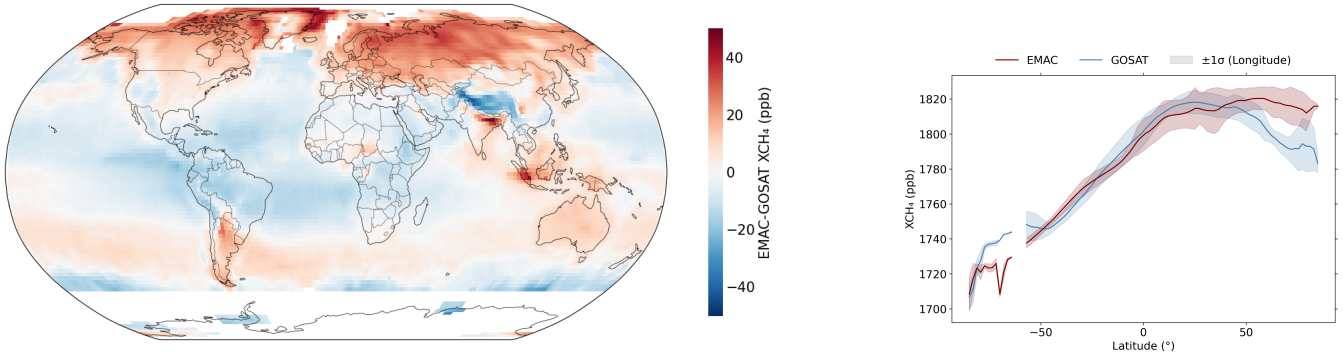

(a) (b)

Figure 5. Comparison of total column modeled and observed CH_4 (XCH_4) data from 2009 to 2019. Panel (a) shows the difference between modeled and observed XCH_4 mixing ratio (EMAC - GOSAT). Panel (b) shows the zonal distribution of XCH_4 based on EMAC model data (red) and GOSAT data (blue).

https://doi.org/10.5194/egusphere-2026-371
Preprint. Discussion started: 10 February 2026

To evaluate soil CH_4 sinks, it is important to use both surface mixing ratio measurements and satellite-derived column-averaged CH_4 (XCH_4). Surface data provide high frequency, local information, but are spatially sparse and can be strongly influenced by local emissions and boundary layer dynamics. In contrast, XCH_4 integrates CH_4 over the full atmospheric column and provides near-global coverage, allowing for a more representative assessment of large-scale soil sink impacts and direct comparison with atmospheric model simulations. Satellite instruments retrieve global XCH_4 data by observing backscattered solar radiation in the shortwave infrared spectrum (Jacob et al., 2022). Specifically, the TANSO-FTS instrument aboard GOSAT has provided continuous global observations of XCH_4 since 2009. In this study, we compare XCH_4 from EMAC simulations with GOSAT for the period from June 2009 to December 2019. The differences in mean XCH_4 between two datasets are illustrated in Figure 5. The global mean difference (EMAC - GOSAT) is 1.78 ppbv, which is notably small compared to the 9.06 ppbv global bias reported for GOSAT XCH_4 relative to TCCON (Parker et al., 2020). This indicates that the XCH_4 simulated by EMAC is in good agreement with satellite observations. Zonal mean comparisons show that in the tropics and mid-latitudes (50°S–50°N), the difference remains within one standard deviation for each latitude band, with largest discrepancies of 6.32 ppbv. However, EMAC simulates higher XCH_4 concentrations compared to GOSAT in the high-latitude regions of the Northern Hemisphere (>50°N), a bias also evident in the zonal mean profile (Figure 5b). These results are consistent with comparisons against ground-based observations, where EMAC also showed higher surface CH_4 concentrations in the Northern Hemisphere high latitudes (Figure 4b). The discrepancy at high latitudes may be partly attributed to sampling limitations and retrieval constraints in the satellite data (Yoshida et al., 2013; Parker et al., 2020). In winter at high latitudes, the number of available GOSAT observations is significantly reduced due to low solar zenith angles and difficulties in retrievals over snow- and ice-covered surfaces (Yoshida et al., 2013; Parker et al., 2020). Whereas EMAC provides a complete dataset for the entire period, the GOSAT mean XCH_4 at high latitudes is calculated from fewer samples compared to the mid-latitudes and tropics. Such seasonal sampling bias likely contributes to the observed inconsistency between EMAC simulations and GOSAT data in these areas, as previously discussed in model-satellite intercomparison studies (e.g., Kivimäki et al. (2019); Massart et al. (2014)). In addition, residual discrepancies may also arise from uncertainties in northern high-latitude natural emissions—particularly wetlands—whose magnitude and seasonality remain among the larger contributors to inter-model spread in global methane budgets (Saunois et al., 2019), as well as from transport-related factors (e.g., stratosphere–troposphere exchange) that can influence column methane at high latitudes (Ostler et al., 2016; Stanevich et al., 2021).

4.2 Comparison of hydrogen mixing ratio against observations

Figure 6 evaluates the performance of the EMAC model using the new online soil sink submodel BIODEP simulating atmospheric H_2. The comparison is based on observations of the NOAA GML Carbon Cycle Cooperative Global Air Sampling Network and model outputs averaged over the 2009–2019 period. Panel (a) shows the spatial distribution of mean modeled H_2 mixing ratios, while panel (b) displays Pearson correlation coefficients (r) between EMAC-modeled and observed H_2 values at individual monitoring stations. The corresponding overview of number of compared data points, mean model and observational H_2 mixing ratio and difference between the model and observational data are listed in Table B1 of the Appendix. The timelines for each station are shown in Figure B2, B3, and B4 of the Appendix.

https://doi.org/10.5194/egusphere-2026-371
Preprint. Discussion started: 10 February 2026

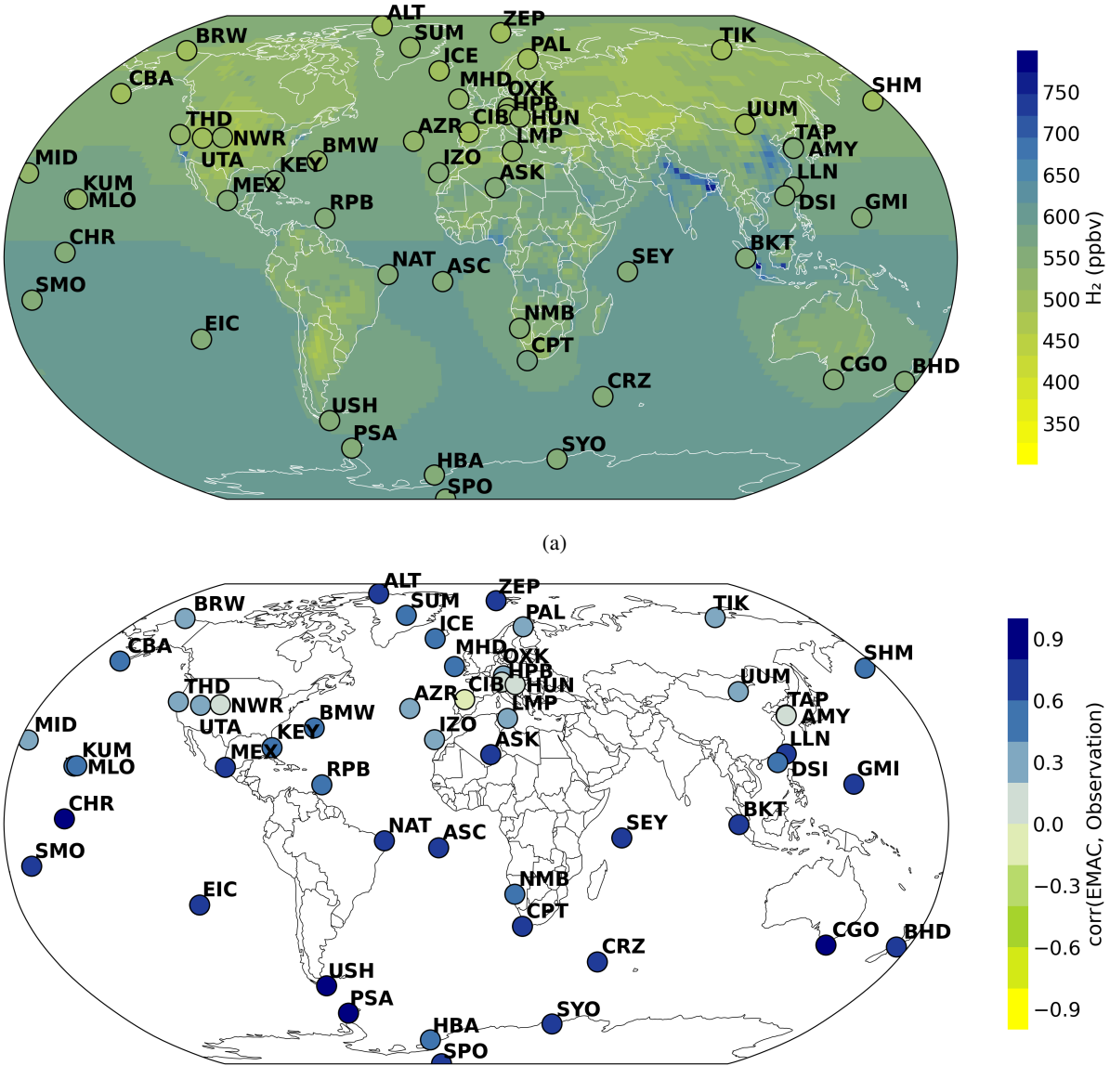

(a)

(b)

Figure 6. Comparison of modeled and observed surface H_2 data. Modeled data are averaged over 2009-2019. Circles indicate observational stations with mid-2020 values estimated using a sixth-order harmonic regression detrended fit. Panel (a) shows the global distribution of mean H_2 mixing ratio (ppbv), and panel (b) shows the corresponding Pearson correlation coefficient between the observation stations and BIODEP results.

Mixing ratios are satisfactorily reproduced for background stations by the EMAC model with correlations higher than $r > 0.60$ for 17 out of 51 stations (Figure 6a). Those stations include for example CHR ($r = 0.86$) or SMO ($r = 0.79$) in the central

https://doi.org/10.5194/egusphere-2026-371
Preprint. Discussion started: 10 February 2026

Pacific Ocean, CPT in South Africa ($r = 0.83$) or PSA in Antarctica ($r = 0.76$). These sites show a comparable seasonal cycle and inter annual variability (see Figure B2), which suggests that the EMAC model with BIODEP accurately represents soil sink dynamics in at remote stations. In these regions, atmospheric dynamics and transport processes tend to be smoother, with more uniform seasonal patterns and comparatively lower biomass burning emissions. This suggests that the EMAC model performs better in regions dominated by large-scale atmospheric transport and stable boundary layer conditions, as these factors minimize sub-grid scale variability. Conversely, there are stations where the seasonal cycle is not well captured by the model, as indicated by low or even negative correlation coefficients between the simulated and observed data. Notable examples include NWR in the United States ($r = 0.01$), HUN in Hungary ($r = 0.11$) or TAP in the Republic of Korea ($r = -0.06$). These stations are mainly located in the continental Northern Hemisphere, where stronger anthropogenic emissions, steep soil sink gradients and more complex boundary layer dynamics are present. The hemispheric seasonal cycles (Figure 7a) indicate that EMAC generally overestimates atmospheric H_2 throughout the year, except during the summer months in the Northern Hemisphere. In the Northern Hemisphere, the simulated seasonal cycle exhibits a slightly larger amplitude than observed, with a maximum in March, whereas the observational data show the maximum occurring in May. In the southern hemisphere, EMAC overestimates H_2 by approximately 30 ppbv throughout the year; however, there is very good agreement in the seasonal cycle. Both data sets exhibit the same cycle, with maximum mixing ratio in winter and minimum mixing ratio in summer, and the phase relationship between the two curves is consistent. The meridional gradient derived from both EMAC model output and observational data, are presented in Figure 7b. Both datasets exhibit a distinct inter hemispheric gradient, with higher H_2 mixing ratios in the Southern Hemisphere. Although H_2 emissions, particularly from fossil fuel combustion, industrial activities, and biomass burning, are stronger in the Northern Hemisphere, this is offset by a correspondingly larger deposition flux, primarily due to more extensive and active soil sink. In contrast, the Southern Hemisphere exhibits a weaker soil sink due to lower landmass coverage, resulting in less efficient H_2 removal. EMAC generally simulates higher H_2 mixing ratios of approximately 30 to 40 ppbv in both hemispheres, with increasing positive bias toward the poles and the smallest model–observation difference occurring near 25°N, where both datasets show mixing ratios of approximately 235 ppbv. In summary, the implementation of the BIODEP submodel within EMAC, allows a realistic simulation of the spatial and seasonal patterns of atmospheric H_2 mixing ratios across diverse regions. High correlations ($r > 0.6$) between modeled and observed values primarily occur at remote, low-emission sites, mainly island or coastal stations in the Southern Hemisphere and the tropics, where large-scale transport dominates and local sub-grid influences are minimal. Conversely, lower or negative correlations occur at mid-latitude locations in the Northern Hemisphere characterized by complex terrain and significant anthropogenic emissions, where enhanced sub-grid variability and unresolved local processes challenge the accuracy of the model. As stated by Surawski et al. (2025), coarse resolution can lead to a limited representation of local and intermittent emission sources, thereby affecting the simulated mixing ratios. These issues related to resolutions are expected to be very pronounced in this study, since the coupled model computes soil moisture data at the same coarse resolution as the EMAC model.

This is much lower than the resolution of the higher-resolution soil moisture datasets such as ERA5. On a global scale, BIODEP estimates an H_2 soil sink of 62.7 ± 11.7 Tg yr^{-1}, which is consistent with previous estimates, including $60.05 \pm$

https://doi.org/10.5194/egusphere-2026-371
Preprint. Discussion started: 10 February 2026

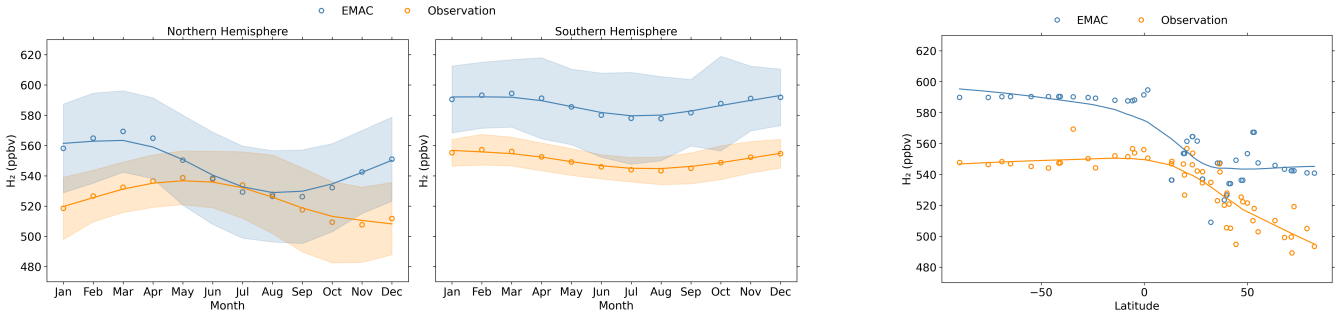

(a) (b)

Figure 7. Comparison of modeled and observed surface H_2 data from June 2009 to December 2019. Solid lines represent smoothed trends obtained using locally estimated scatterplot smoothing (LOESS) with a smoothing parameter of 2/3 and locally linear fitting. Panel (a) shows the seasonal variability of modeled and observed H_2 data. Shaded areas represent the temporal standard deviations. Panel (b) shows the meridional distribution of H_2 based on EMAC model outputs and observational data from stations with at least 12 monthly measurements.

0.07 Tg yr^{-1} (Surawski et al., 2025), 44–73 Tg yr^{-1} (Sand et al., 2023), 57–60 $\pm$ 12 Tg yr^{-1} (Yashiro et al., 2011), and 60^{+30}_{-20} Tg yr^{-1} (Ehhalt and Rohrer, 2009).

4.3 Dependence of soil gas uptake on temperature and moisture

Table 4 summarizes the soil temperature and moisture conditions associated with maximum uptake of CH_4 and H_2, together with 95% bootstrap confidence intervals. Maximum CH_4 uptake occurs at a mean soil temperature of 37.48,°C and low moisture conditions (SM = 0.087), whereas H_2 uptake peaks at a slightly higher optimal temperature of 41.39,°C and at comparatively higher soil moisture (SM = 0.222). Figure 8 presents the two-dimensional heatmaps of mean soil uptake rates from the model results for CH_4 (panel a) and H_2 (panel b), as well as the corresponding data density (panel c), shown as a function of soil temperature (T_{soil}) and volumetric soil moisture (SM). CH_4 uptake increases with temperature up to approximately 35–43,°C and is highest at soil moisture fractions between 0.09 and 0.27. H_2 uptake displays a similar pattern, but with its maximum uptake range broadened between 35–43,°C and slightly larger soil moisture (0.19-0.43). The data density map (panel c) indicates that prevalent conditions are at moderate temperatures (2–28,°C) and moisture fractions between 0.2 and 0.4, with substantially fewer data points available under hot and very dry or very wet conditions. These results highlight that, although both gases exhibit enhanced uptake under warm conditions, their moisture optima differ.

Table 4. Soil temperature and moisture conditions corresponding to maximum H_2 and CH_4 uptake, with 95% bootstrap confidence intervals.

Gas	T_{soil} (°C)	95% CI (°C)	SM	95% CI
CH_4	37.48	[35.53, 43.35]	0.087	[0.088, 0.268]
H_2	41.39	[27.71, 43.35]	0.222	[0.193, 0.430]

https://doi.org/10.5194/egusphere-2026-371
Preprint. Discussion started: 10 February 2026

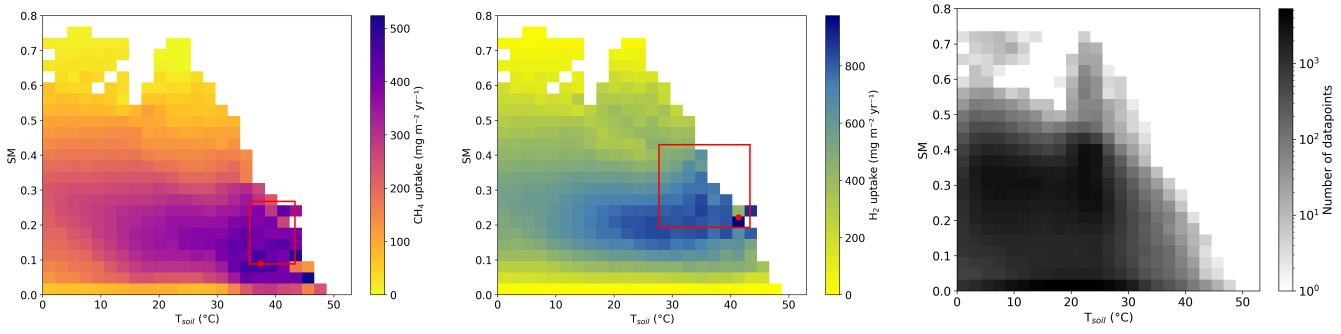

(a) (b) (c)

Figure 8. Heatmaps derived from model results of mean gas uptake and data density versus soil temperature (T_{soil}, °C) and soil moisture (SM). (a) CH_4 uptake, (b) H_2 uptake, and (c) number of modeled data points. Darker colors indicate higher uptake or larger counts. Red boxes in panels (a) and (b) represent the 95% bootstrap confidence intervals associated with the largest uptake rates and their corresponding optimal soil temperature and moisture conditions, while the red dot denotes the maximum uptake rate.

5 Conclusions

Implementing the BIODEP (v1.0) soil sink submodel into the MESSy framework and coupling it to EMAC has enabled a consistent, online representation of global atmospheric H_2 and CH_4 deposition. In combination with prescribed emissions and online chemistry, this setup allows an interactive simulation of these important long-lived tracers, including their large-scale spatial patterns and the inter-hemispheric gradients. A comparison with GOSAT CH_4 observations shows that the EMAC model accurately reproduces global and zonal mean column methane distributions. Deviations are largely confined to the high latitudes of the Northern Hemisphere, where the effects of satellite sampling limitations and emission uncertainties are expected. For H_2, in the Southern Hemisphere, where background conditions dominate, EMAC reproduces both the seasonal cycles and spatial distributions particularly well, although a persistent positive bias of approximately 30 ppbv remains. On the other side, in the Northern Hemisphere, the model captures the general shape of the observed seasonal cycles, but displays systematic overestimation for both gases, a larger amplitude in the H_2 cycle, and a shift in the timing of seasonal extrema relative to observations. These discrepancies are most pronounced at mid- and high-latitude stations, where complex terrain, stronger anthropogenic influence, and sub-grid-scale processes such as local emissions and soil moisture variability are not fully represented by the model. The analysis of soil drivers such as temperature and moisture demonstrates EMAC's ability to reproduce the soil sinks of both gases in line with the temperature- and moisture-dependent uptake algorithms described by Surawski et al. (2025) for hydrogen and Murguia-Flores et al. (2018) for methane. Despite regional limitations, the model produces globally soil uptake estimates of 62.7 ± 11.7 Tg yr^{-1} for H_2 and 30.2 ± 4.8 Tg yr^{-1} for CH_4, both values lying within the range of previous studies. The combined evaluation of global distributions, hemispheric seasonal cycles, and soil environmental controls demonstrates that EMAC, coupled with the BIODEP scheme, provides a robust framework for assessing the atmospheric budgets and soil–atmosphere exchange processes of these trace gases, while indicating where future improve-

https://doi.org/10.5194/egusphere-2026-371
Preprint. Discussion started: 10 February 2026

ments, particularly in spatial resolution and emission inventories, would further enhance model performance. By incorporating BIODEP, EMAC now uniquely enables interactive online simulations of CH_4 soil sinks fully coupled with the H_2 cycle and atmospheric chemistry.

https://doi.org/10.5194/egusphere-2026-371
Preprint. Discussion started: 10 February 2026

Appendix A: Methane

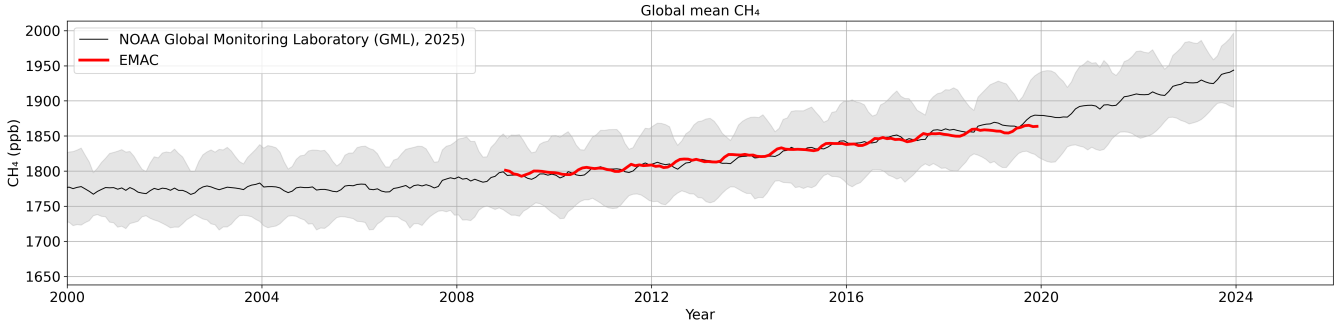

Figure A1. Global mean observations of CH_4 from the NOAA Global Monitoring Laboratory (NOAA Global Monitoring Laboratory (GML), 2025) (black), compared with the CH_4trend simulated by EMAC (red). Shaded areas represent the spatial standard deviation.

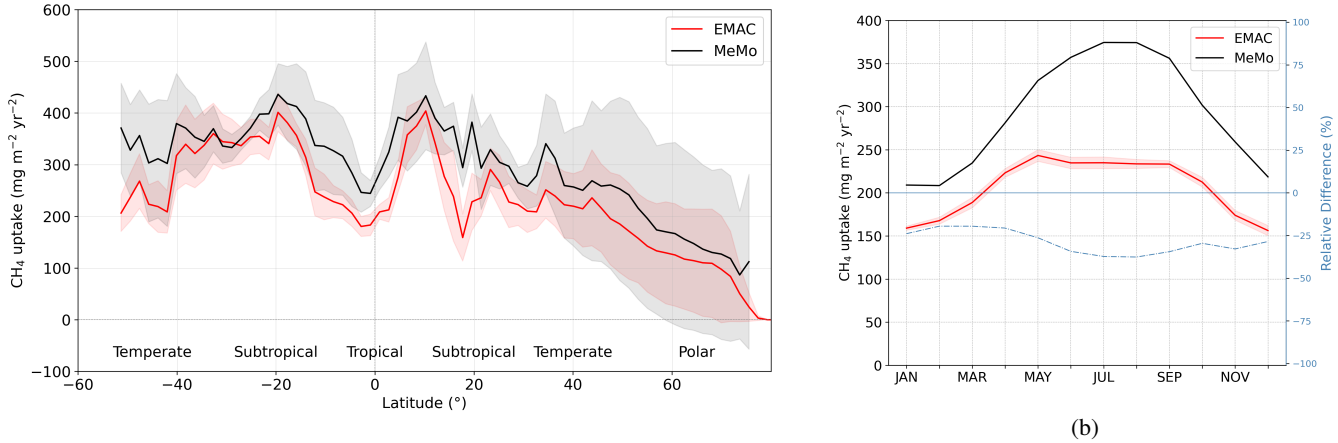

(a) (b)

Figure A2. Mean distribution of CH_4 uptake (in mg m^{-2} yr^{-1}) averaged over the period 2009-2019 from the new BIODEP submodel coupled to EMAC/JSBACH (red) and from the MeMo average for 2000 (black). Shaded areas indicate the standard deviation for each dataset. Panel (a) shows the latitudinal distribution and panel (b) the monthly distribution.

https://doi.org/10.5194/egusphere-2026-371
Preprint. Discussion started: 10 February 2026

Table A1. Comparison of mean model and observational CH_4 mixing ratios. Δ = Model − Observed, while r denotes the Pearson correlation coefficient.

Station	Longitude	Latitude	# values	CH_4 EMAC (ppbv)	CH_4 Observed (ppbv)	Δ (ppbv)	r
ALT	-62.50	82.50	131	1908.6	1908.3	0.28	0.70
AMY	126.00	36.50	71	2032.9	1959.6	73.26	-0.25
ASC	-14.40	-7.97	131	1784.8	1789.3	-4.50	0.97
ASK	5.63	23.30	127	1859.5	1857.5	1.99	0.96
AZR	-27.40	38.80	102	1879.9	1887.3	-7.40	0.92
BHD	175.00	-41.40	123	1790.0	1781.2	8.78	0.96
BKT	100.00	-0.20	108	1939.6	1859.8	79.75	0.68
BMW	-64.90	32.30	128	1878.7	1878.5	0.18	0.88
BRW	-157.00	71.30	131	1912.9	1919.4	-6.46	0.77
CBA	-163.00	55.20	121	1900.8	1907.4	-6.64	0.84
CGO	145.00	-40.70	131	1787.7	1778.3	9.43	0.96
CHR	-157.00	1.70	98	1794.0	1802.0	-8.03	0.92
CIB	-4.93	41.80	126	1928.8	1913.3	15.59	0.83
CPT	18.50	-34.40	116	1798.5	1784.1	14.41	0.91
CRZ	51.80	-46.40	130	1780.5	1777.2	3.25	0.97
DSI	117.00	20.70	112	1912.7	1888.5	24.19	0.55
EIC	-109.00	-27.20	117	1775.4	1776.0	-0.66	0.96
GMI	145.00	13.40	114	1831.7	1834.9	-3.18	0.88
HBA	-26.20	-75.60	97	1768.6	1765.5	3.05	0.95
HPB	11.00	47.80	131	1996.4	1947.0	49.47	0.63
HUN	16.70	47.00	131	2038.2	1956.7	81.46	0.53
ICE	-20.30	63.40	128	1911.8	1903.2	8.65	0.68
IZO	-16.50	28.30	131	1876.6	1862.4	14.23	0.88
KEY	-80.20	25.70	131	1920.7	1870.3	50.39	0.77
KUM	-155.00	19.60	131	1848.6	1857.5	-8.89	0.93
LLN	121.00	23.50	131	1884.9	1863.3	21.57	0.74
LMP	12.60	35.50	131	1922.2	1900.5	21.70	0.81
MEX	-97.30	19.00	131	1885.2	1844.4	40.86	0.80
MHD	-9.90	53.30	131	1925.6	1898.4	27.21	0.79
MID	-177.00	28.20	131	1863.4	1870.4	-6.94	0.94
MLO	-156.00	19.50	131	1848.6	1841.9	6.72	0.94
NAT	-35.20	-5.68	104	1802.4	1802.4	-0.05	0.93
NMB	15.00	-23.60	125	1794.8	1789.1	5.67	0.96
NWR	-106.00	40.10	131	1960.4	1876.8	83.59	0.78
OXK	11.80	50.00	125	2004.8	1930.3	74.46	0.57
PAL	24.10	68.00	131	2007.8	1923.8	84.07	0.05
PSA	-64.10	-64.80	131	1780.5	1776.8	3.70	0.97
RPB	-59.40	13.20	131	1831.5	1845.8	-14.35	0.97
SEY	55.50	-4.68	131	1800.7	1803.4	-2.64	0.93
SHM	174.00	52.70	124	1899.9	1904.4	-4.48	0.82
SMO	-171.00	-14.20	131	1782.5	1785.0	-2.44	0.97
SPO	-24.80	-89.50	131	1779.6	1776.9	2.74	0.97
SUM	-38.40	72.60	131	1894.6	1899.0	-4.43	0.89
SYO	39.60	-69.00	131	1780.1	1776.8	3.30	0.97
TAP	126.00	36.70	131	2010.0	1940.4	69.63	0.30
THD	-124.00	41.10	101	1874.7	1881.1	-6.42	0.84
TIK	129.00	71.60	77	1942.3	1938.7	3.60	0.38
USH	-68.30	-54.80	127	1781.3	1777.7	3.63	0.97
UTA	-114.00	39.90	131	1890.1	1883.4	6.74	0.85
UUM	111.00	44.50	131	1910.5	1907.5	2.94	0.85
ZEP	11.90	78.90	131	1925.2	1910.3	14.85	0.49

https://doi.org/10.5194/egusphere-2026-371
Preprint. Discussion started: 10 February 2026

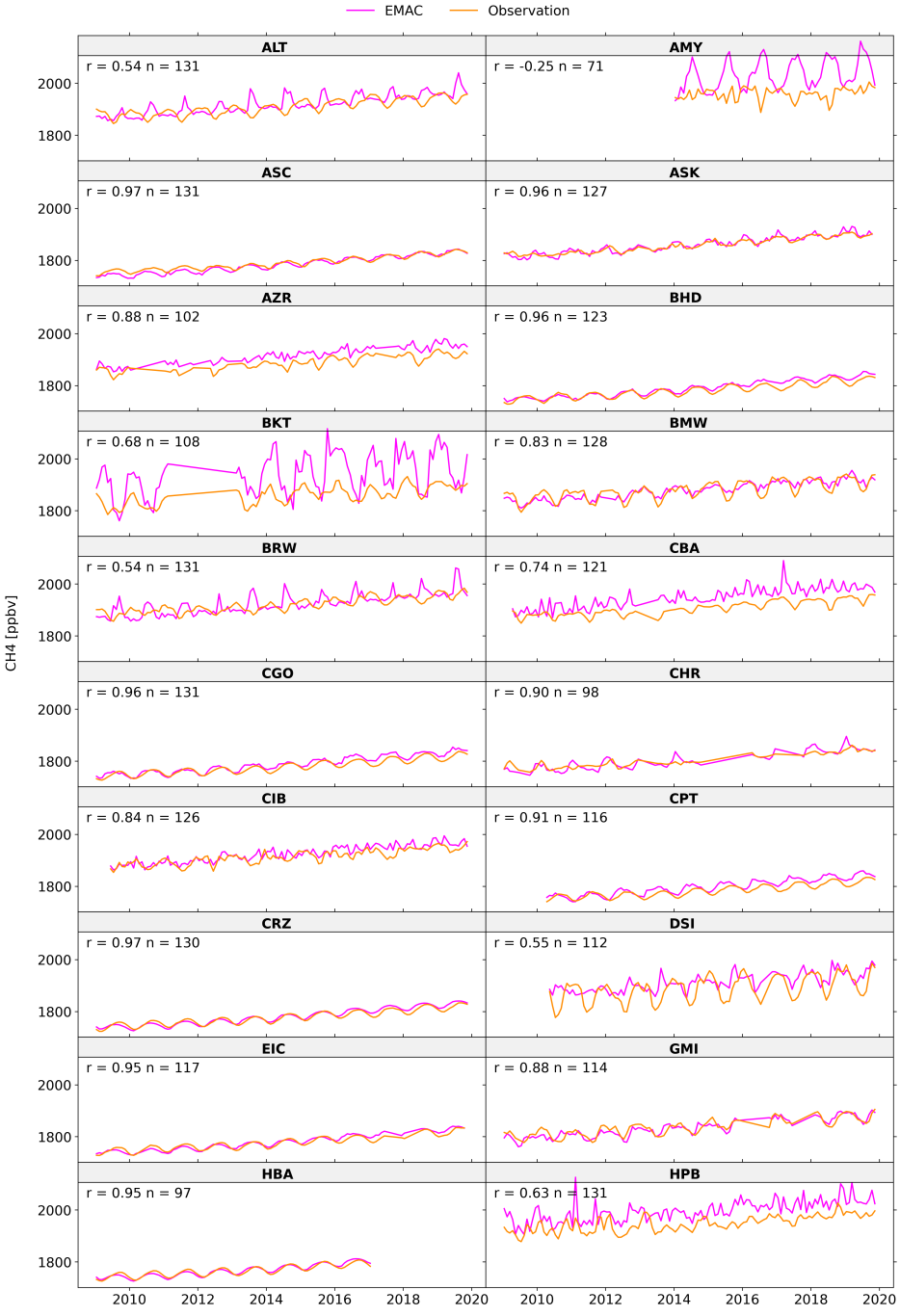

Figure A3. Comparison of CH_4 time series from observations and the EMAC model at 20 of the 51 stations with complete monthly data between 2009-2019. The number of observational data points is indicated by n, and r represents the Pearson correlation coefficient between observed and modeled values.

https://doi.org/10.5194/egusphere-2026-371
Preprint. Discussion started: 10 February 2026

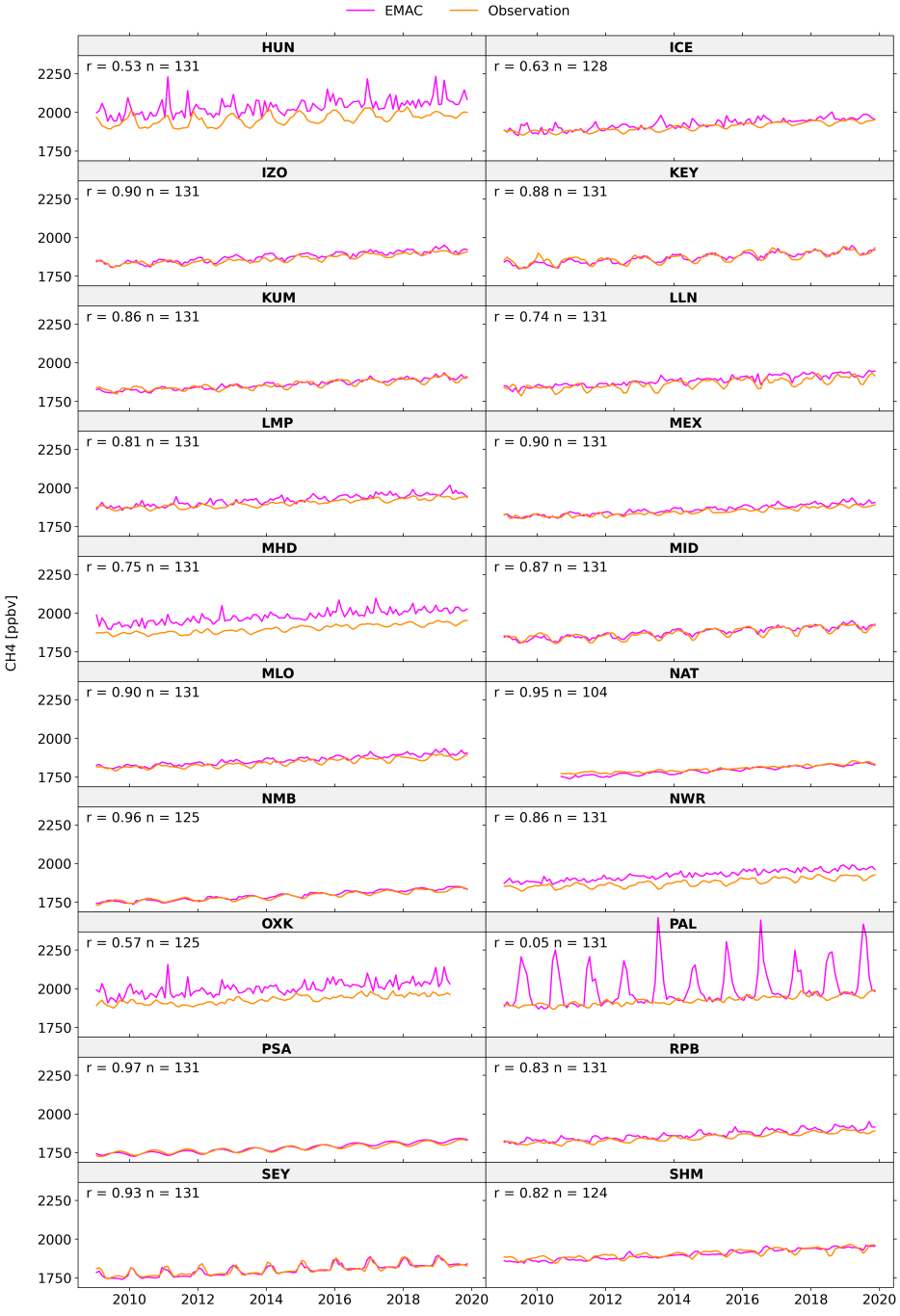

Figure A4. Comparison of CH_4 time series from observations and the EMAC model at 20 of the 51 stations. The number of observational data points is indicated by n, and r represents the Pearson correlation coefficient between observed and modeled values, part 2

https://doi.org/10.5194/egusphere-2026-371
Preprint. Discussion started: 10 February 2026

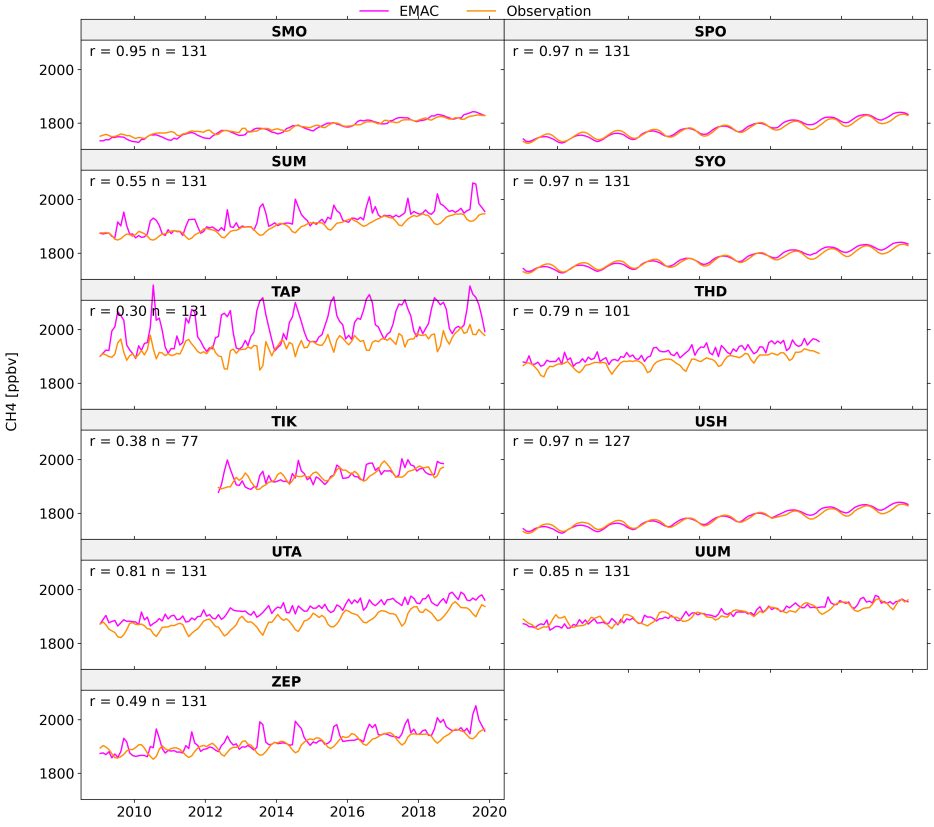

Figure A5. Comparison of CH_4 time series from observations and the EMAC model at 11 of the 51 stations. The number of observational data points is indicated by n, and r represents the Pearson correlation coefficient between observed and modeled values, part 3

https://doi.org/10.5194/egusphere-2026-371
Preprint. Discussion started: 10 February 2026

Appendix B: Hydrogen

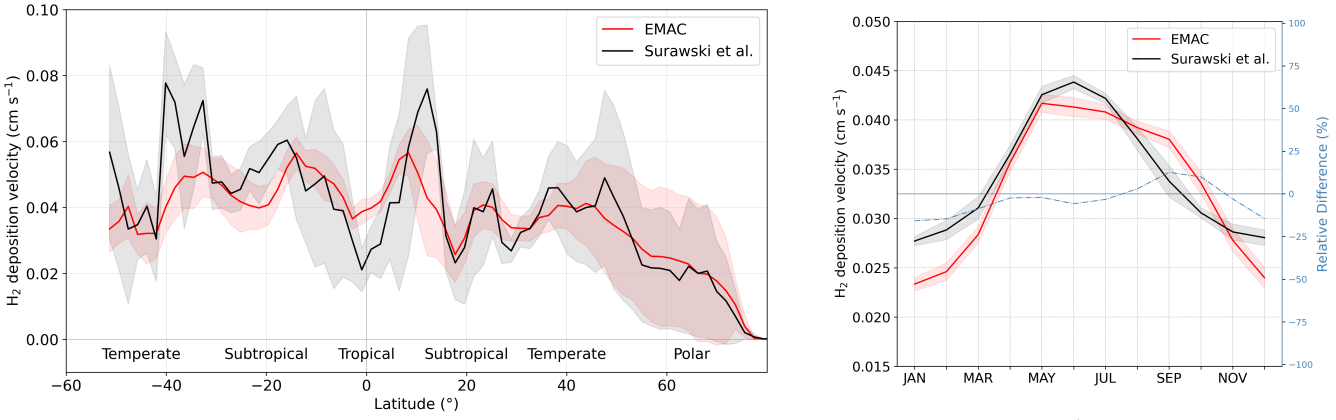

(a) (b)

Figure B1. Mean distribution of H_2 deposition velocity (in cm s^{-1}) averaged over the period 2009-2019 from the new BIODEP submodel coupled to EMAC/JSBACH (red) and from the Surawski et al. (2025) average for 2000 (black). Shaded areas indicate the standard deviation for each dataset. Panel (a) shows the latitudinal distribution and panel (b) the monthly distribution.

https://doi.org/10.5194/egusphere-2026-371
Preprint. Discussion started: 10 February 2026

Table B1. Comparison of mean model and observational H_2 mixing ratios. Δ = Model − Observed, while r denotes the Pearson correlation coefficient.

Station	Longitude	Latitude	# values	H_2 EMAC (ppbv)	H_2 Observed (ppbv)	Δ (ppbv)	r
ALT	-62.50	82.50	123	544.9	493.4	51.47	0.67
AMY	126.00	36.50	71	569.9	547.3	22.64	0.07
ASC	-14.40	-7.97	118	593.9	551.4	42.57	0.67
ASK	5.63	23.30	117	563.6	546.2	17.39	0.63
AZR	-27.40	38.80	98	564.0	520.2	43.82	0.21
BHD	175.00	-41.40	102	589.8	547.1	42.71	0.78
BKT	100.00	-0.20	93	610.7	556.1	54.62	0.67
BMW	-64.90	32.30	118	567.9	534.9	33.00	0.44
BRW	-157.00	71.30	121	538.7	499.6	39.10	0.34
CBA	-163.00	55.20	114	550.1	502.9	47.19	0.40
CGO	145.00	-40.70	120	586.8	547.4	39.42	0.81
CHR	-157.00	1.70	83	592.5	550.4	42.10	0.86
CIB	-4.93	41.80	121	527.5	505.4	22.10	-0.06
CPT	18.50	-34.40	105	593.2	569.1	24.13	0.79
CRZ	51.80	-46.40	118	592.5	544.0	48.41	0.80
DSI	117.00	20.70	112	592.7	556.8	35.85	0.47
EIC	-109.00	-27.20	108	594.7	550.2	44.53	0.72
GMI	145.00	13.40	102	586.6	548.4	38.11	0.62
HBA	-26.20	-75.60	96	584.9	546.4	38.55	0.59
HPB	11.00	47.80	120	540.6	522.3	18.31	0.16
HUN	16.70	47.00	124	523.9	525.5	-1.59	0.11
ICE	-20.30	63.40	122	549.2	510.2	39.05	0.56
IZO	-16.50	28.30	124	561.2	541.7	19.56	0.31
KEY	-80.20	25.70	121	585.4	542.3	43.07	0.59
KUM	-155.00	19.60	121	579.9	526.6	53.32	0.49
LLN	121.00	23.50	120	585.3	553.8	31.53	0.73
LMP	12.60	35.50	122	554.7	523.1	31.60	0.23
MEX	-97.30	19.00	120	561.3	546.7	14.60	0.65
MHD	-9.90	53.30	125	548.0	518.0	30.01	0.43
MID	-177.00	28.20	122	571.6	534.6	36.96	0.33
MLO	-156.00	19.50	121	579.9	539.6	40.23	0.42
NAT	-35.20	-5.68	102	590.2	556.5	33.67	0.63
NMB	15.00	-23.60	113	537.4	544.1	-6.71	0.50
NWR	-106.00	40.10	121	525.1	528.0	-2.93	0.01
OXK	11.80	50.00	116	535.8	521.5	14.31	0.26
PAL	24.10	68.00	122	523.3	499.2	24.14	0.26
PSA	-64.10	-64.80	125	591.9	546.8	45.16	0.83
RPB	-59.40	13.20	120	586.1	546.9	39.12	0.53
SEY	55.50	-4.68	123	595.8	553.8	42.06	0.65
SHM	174.00	52.70	111	546.3	510.1	36.15	0.45
SMO	-171.00	-14.20	121	596.2	551.9	44.30	0.79
SPO	-24.80	-89.50	128	590.7	547.6	43.16	0.71
SUM	-38.40	72.60	125	554.3	519.2	35.11	0.44
SYO	39.60	-69.00	129	590.9	548.1	42.75	0.73
TAP	126.00	36.70	123	561.8	541.8	19.95	-0.06
THD	-124.00	41.10	91	526.9	520.8	6.10	0.21
TIK	129.00	71.60	75	527.9	489.2	38.64	0.22
USH	-68.30	-54.80	118	583.8	545.1	38.75	0.80
UTA	-114.00	39.90	121	525.5	505.8	19.63	0.32
UUM	111.00	44.50	123	512.9	495.0	17.92	0.23
ZEP	11.90	78.90	123	542.0	505.0	37.04	0.60

https://doi.org/10.5194/egusphere-2026-371
Preprint. Discussion started: 10 February 2026

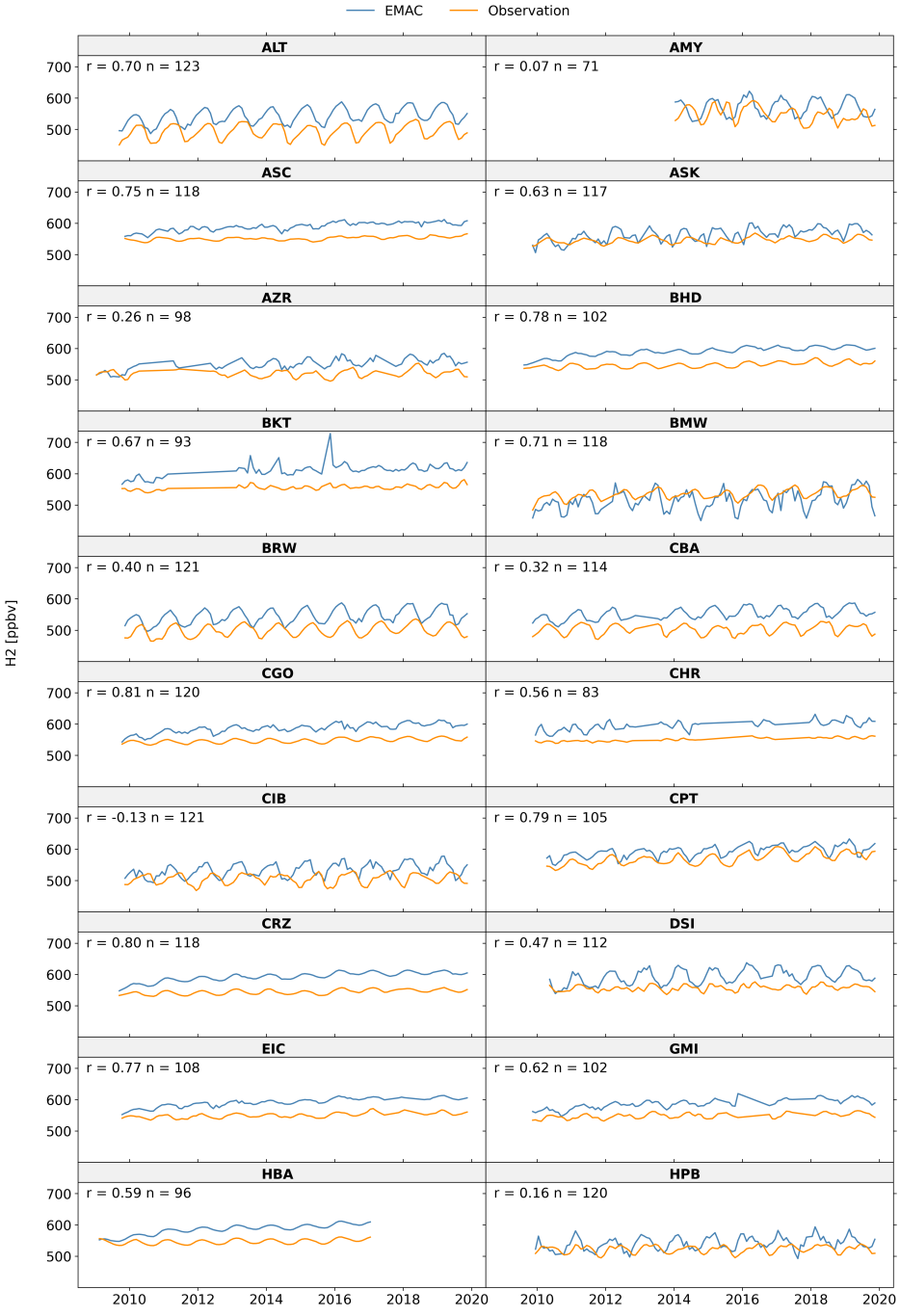

Figure B2. Comparison of H_2 time series from observations and the EMAC model at 20 of the 51 stations with complete monthly data between 2009-2019. The number of observational data points is indicated by n, and r represents the Pearson correlation coefficient between observed and modeled values.

https://doi.org/10.5194/egusphere-2026-371
Preprint. Discussion started: 10 February 2026

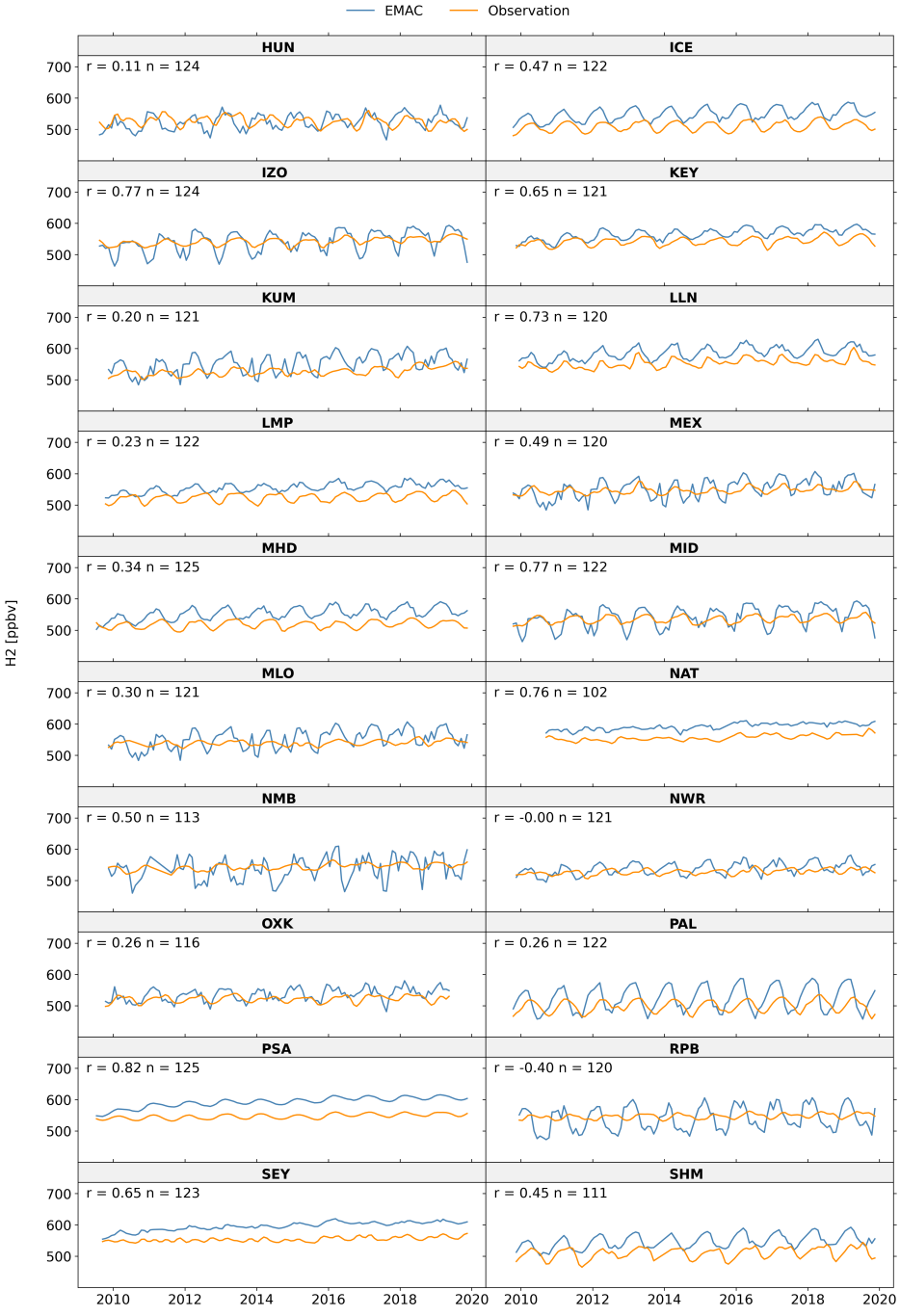

Figure B3. Comparison of H_2 time series from observations and the EMAC model at 20 of the 51 stations. The number of observational data points is indicated by n, and r represents the Pearson correlation coefficient between observed and modeled values, part 2

https://doi.org/10.5194/egusphere-2026-371
Preprint. Discussion started: 10 February 2026

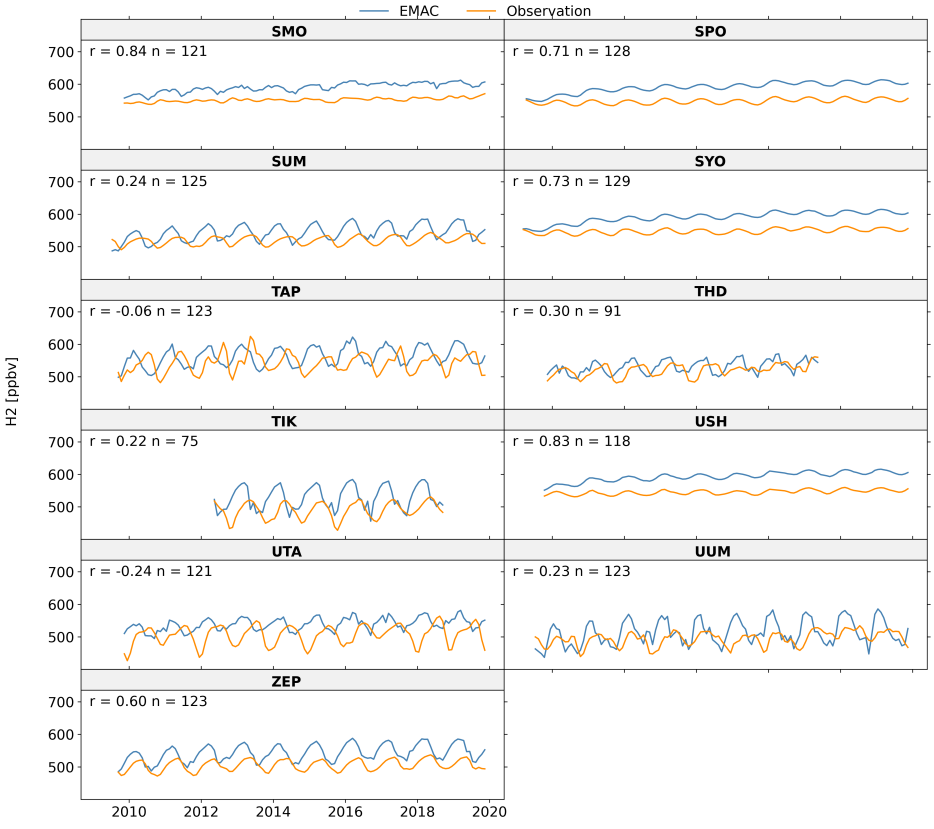

Figure B4. Comparison of H_2 time series from observations and the EMAC model at 11 of the 51 stations. The number of observational data points is indicated by n, and r represents the Pearson correlation coefficient between observed and modeled values, part 3

https://doi.org/10.5194/egusphere-2026-371
Preprint. Discussion started: 10 February 2026

Code availability. The Modular Earth Submodel System (MESSy, https://doi.org/10.5281/zenodo.8360186) is continuously further developed and applied by a consortium of institutions. The usage of MESSy and access to the source code is licenced to all affiliates of institutions which are members of the MESSy Consortium. Institutions can become a member of the MESSy Consortium by signing the MESSy Memorandum of Understanding. More information can be found on the MESSy Consortium Website (http://www.messy-interface.org). The exact version of the EMAC v2.55.2 source code and simulation set-ups used to produce the results used in this paper is archived on the Zenodo repository at https://zenodo.org/records/18327501 (The MESSy Consortium, 2025).

Data availability. Sand and loess loam fractions are taken from the LDAS/GLDAS data sets (Rodell et al., 2004). Clay fraction and bulk density are available from the global soil dataset http://globalchange.bnu.edu.cn/research/soilw (Shangguan et al., 2014). Anthropogenic nitrogen from fertilizers is available at https://doi.pangaea.de/10.1594/PANGAEA.861203 (Nishina et al., 2017). The ERA5 reanalysis data can be accessed at https://doi.org/10.24381/cds.adbb2d47 (Hersbach et al., 2023), and the Global Fire Emissions Database (GFED) v4.1 is available at https://doi.org/10.3334/ORNLDAAC/1293 (Randerson et al., 2017). The NOAA GML Carbon Cycle Cooperative Global Air Sampling Network data are available at https://doi.org/10.15138/WP0W-EZ08 (Pétron et al., 2024) and https://doi.org/10.15138/VNCZ-M766 (Lan et al., 2025).

Author contributions. AM and AP planned the research. AM developed the submodel code and performed the simulations. AP, KK, BS and SG contributed to the overall submodel and setup development. KK provided the H_2 station observation datasets. BS provided the CH_4 station observation datasets. NS provided H_2 deposition datasets. YL, DC and SJ provided the XCH_4 satellite observation datasets. AM, YL and DC wrote the manuscript. AP and JL supervised the project. All authors discussed the results and contributed to the writing and editing of the manuscript.

Competing interests. At least one of the (co-)authors is a member of the editorial board of Geoscientific Model Development.

Acknowledgements. The model simulations have been performed at the German Climate Computing Centre (DKRZ) through support from the Max Planck Society. This work was supported by the Max Planck Graduate Center with the Johannes Gutenberg-Universität Mainz (MPGC).

https://doi.org/10.5194/egusphere-2026-371
Preprint. Discussion started: 10 February 2026

References

Aronson, E. and Helliker, B.: Methane flux in non-wetland soils in response to nitrogen addition: a meta-analysis, Ecology, 91, 3242–3251, 2010.

Berrisford, P., Dee, D., Poli, P., Brugge, R., Fielding, M., Fuentes, M., Kållberg, P., Kobayashi, S., Uppala, S., and Simmons, A.: The ERA-Interim archive Version 2.0, Shinfield Park, Reading, 2011.

Bradford, M., Ineson, P., Wookey, P., and Lappin-Scott, H.: The effects of acid nitrogen and acid sulphur deposition on CH4 oxidation in a forest soil: a laboratory study, Soil Biology and Biochemistry, 33, 1695–1702, 2001.

Bronson, K. and Mosier, A.: Suppression of methane oxidation in aerobic soil by nitrogen fertilizers, nitrification inhibitors, and urease inhibitors, Biology and Fertility of Soils, 17, 263–268, 1994.

Butterbach-Bahl, K. and Papen, H.: Four years continuous record of CH 4-exchange between the atmosphere and untreated and limed soil of a N-saturated spruce and beech forest ecosystem in Germany, Plant and Soil, 240, 77–90, 2002.

Cai, Z. C. and Mosier, A. R.: Effect of NH4Cl addition on methane oxidation by paddy soils, Soil Biology and Biochemistry, 32, 1537–1545, 2000.

Castro, M. S., Steudler, P. A., Melillo, J. M., Aber, J. D., and Bowden, R. D.: Factors controlling atmospheric methane consumption by temperate forest soils, Global biogeochemical cycles, 9, 1–10, 1995.

Constant, P., Poissant, L., and Villemur, R.: Tropospheric H2 budget and the response of its soil uptake under the changing environment, Science of the Total Environment, 407, 1809–1823, 2009.

Curry, C. L.: Modeling the soil consumption of atmospheric methane at the global scale, Global Biogeochemical Cycles, 21, 2007.

De Visscher, A. and Van Cleemput, O.: Induction of enhanced CH4 oxidation in soils: NH4+ inhibition patterns, Soil Biology and Biochemistry, 35, 907–913, 2003.

Derwent, R. G. and Jenkin, M. E.: Estimation of the atmospheric hydrogen source from the oxidation of man-made and natural non-methane organic compounds using a Master Chemical Mechanism, Atmospheric Environment, 339, 120 871, 2024.

Dutaur, L. and Verchot, L. V.: A global inventory of the soil CH4 sink, Global biogeochemical cycles, 21, 2007.

Ehhalt, D. and Rohrer, F.: The tropospheric cycle of H2: a critical review, Tellus B: Chemical and Physical Meteorology, 61, 500–535, 2009.

Ehhalt, D. and Rohrer, F.: Deposition velocity of H2: a new algorithm for its dependence on soil moisture and temperature, Tellus B: Chemical and Physical Meteorology, 65, 19 904, 2013.

Grosso, S. D., Parton, W., Mosier, A., Ojima, D., Potter, C., Borken, W., Brumme, R., Butterbach-Bahl, K., Crill, P., Dobbie, K., et al.: General CH4 oxidation model and comparisons of CH4 oxidation in natural and managed systems, Global Biogeochemical Cycles, 14, 999–1019, 2000.

Gulledge, J. and Schimel, J. P.: Low-concentration kinetics of atmospheric CH4 oxidation in soil and mechanism of NH4+ inhibition, Applied and Environmental Microbiology, 64, 4291–4298, 1998.

Hagemann, S. and Stacke, T.: Impact of the soil hydrology scheme on simulated soil moisture memory, Climate Dynamics, 44, 1731–1750, https://doi.org/10.1007/s00382-014-2221-6, 2015.

Hauglustaine, D., Paulot, F., Collins, W., Derwent, R., Sand, M., and Boucher, O.: Climate benefit of a future hydrogen economy, Communications Earth & Environment, 3, 295, 2022.

https://doi.org/10.5194/egusphere-2026-371
Preprint. Discussion started: 10 February 2026

Hersbach, H., Bell, B., Berrisford, P., Biavati, G., Horányi, A., Muñoz Sabater, J., Nicolas, J., Peubey, C., Radu, R., Rozum, I., Schepers, D., Simmons, A., Soci, C., Dee, D., and Thépaut, J.-N.: ERA5 hourly data on single levels from 1940 to present, Copernicus Climate Change Service (C3S) Climate Data Store (CDS) (last access: 19 September 2024), https://doi.org/10.24381/cds.adbb2d47, 2023.

Houweling, S., Kaminski, T., Dentener, F., Lelieveld, J., and Heimann, M.: Inverse modeling of methane sources and sinks using the adjoint of a global transport model, Journal of Geophysical Research: Atmospheres, 104, 26 137–26 160, 1999.

IPCC: Climate Change 2023: Synthesis Report. Contribution of Working Groups I, II and III to the Sixth Assessment Report of the Intergovernmental Panel on Climate Change, IPCC, Geneva, Switzerland, https://doi.org/10.59327/IPCC/AR6-9789291691647, 2023.

Ito, A. and Inatomi, M.: Use of a process-based model for assessing the methane budgets of global terrestrial ecosystems and evaluation of uncertainty, Biogeosciences, 9, 759–773, 2012.

Jacob, D. J., Varon, D. J., Cusworth, D. H., Dennison, P. E., Frankenberg, C., Gautam, R., Guanter, L., Kelley, J., McKeever, J., Ott, L. E., et al.: Quantifying methane emissions from the global scale down to point sources using satellite observations of atmospheric methane, Atmospheric Chemistry and Physics Discussions, 2022, 1–44, 2022.

Jeuken, A., Siegmund, P., Heijboer, L., Feichter, J., and Bengtsson, L.: On the potential of assimilating meteorological analyses in a global climate model for the purpose of model validation, Journal of Geophysical Research: Atmospheres, 101, 16 939–16 950, 1996.

Jöckel, P., Tost, H., Pozzer, A., Brühl, C., Buchholz, J., Ganzeveld, L., Hoor, P., Kerkweg, A., Lawrence, M., Sander, R., et al.: The atmospheric chemistry general circulation model ECHAM5/MESSy1: consistent simulation of ozone from the surface to the mesosphere, Atmospheric Chemistry and Physics, 6, 5067–5104, 2006.

Jöckel, P., Kerkweg, A., Pozzer, A., Sander, R., Tost, H., Riede, H., Baumgaertner, A., Gromov, S., and Kern, B.: Development cycle 2 of the Modular Earth Submodel System (MESSy2), Geoscientific Model Development, 3, 717–752, https://doi.org/10.5194/gmd-3-717-2010, 2010.

Jöckel, P., Tost, H., Pozzer, A., Kunze, M., Kirner, O., Brenninkmeijer, C. A. M., Brinkop, S., Cai, D. S., Dyroff, C., Eckstein, J., Frank, F., Garny, H., Gottschaldt, K.-D., Graf, P., Grewe, V., Kerkweg, A., Kern, B., Matthes, S., Mertens, M., Meul, S., Neumaier, M., Nützel, M., Oberländer-Hayn, S., Ruhnke, R., Runde, T., Sander, R., Scharffe, D., and Zahn, A.: Earth System Chemistry integrated Modelling (ESCiMo) with the Modular Earth Submodel System (MESSy) version 2.51, Geoscientific Model Development, 9, 1153–1200, https://doi.org/10.5194/gmd-9-1153-2016, 2016.

Kerkweg, A., Sander, R., Tost, H., and Jöckel, P.: Implementation of prescribed (OFFLEM), calculated (ONLEM), and pseudo-emissions (TNUDGE) of chemical species in the Modular Earth Submodel System (MESSy), Atmospheric Chemistry and Physics, 6, 3603–3609, 2006.

Kivimäki, E., Lindqvist, H., Hakkarainen, J., Laine, M., Sussmann, R., Tsuruta, A., Detmers, R., Deutscher, N. M., Dlugokencky, E. J., Hase, F., et al.: Evaluation and analysis of the seasonal cycle and variability of the trend from GOSAT methane retrievals, Remote Sensing, 11, 882, 2019.

Kleinen, T., Mikolajewicz, U., and Brovkin, V.: Terrestrial methane emissions from the Last Glacial Maximum to the preindustrial period, Climate of the Past, 16, 575–595, 2020.

Kohl, M., Lelieveld, J., Chowdhury, S., Ehrhart, S., Sharma, D., Cheng, Y., Tripathi, S. N., Sebastian, M., Pandithurai, G., Wang, H., et al.: Numerical simulation and evaluation of global ultrafine particle concentrations at the Earth's surface, EGUsphere, 2023, 1–34, 2023.

Kuze, A., Suto, H., Nakajima, M., and Hamazaki, T.: Thermal and near infrared sensor for carbon observation Fourier-transform spectrometer on the Greenhouse Gases Observing Satellite for greenhouse gases monitoring, Applied optics, 48, 6716–6733, 2009.

https://doi.org/10.5194/egusphere-2026-371
Preprint. Discussion started: 10 February 2026

Lan, X., Mund, J., Crotwell, A., Thoning, K., Moglia, E., Madronich, M., Baugh, K., Petron, G., Crotwell, M., Neff, D., Wolter, S., Mefford, T., and DeVogel, S.: Atmospheric Methane Dry Air Mole Fractions from the NOAA GML Carbon Cycle Cooperative Global Air Sampling Network, 1983–2024, https://doi.org/10.15138/VNCZ-M766, accessed YYYY-MM-DD, 2025.

Luo, G., Kiese, R., Wolf, B., and Butterbach-Bahl, K.: Effects of soil temperature and moisture on methane uptake and nitrous oxide emissions across three different ecosystem types, Biogeosciences, 10, 3205–3219, 2013.

MacDonald, J. A., Skiba, U., Sheppard, L. J., Hargreaves, K. J., Smith, K. A., and Fowler, D.: Soil environmental variables affecting the flux of methane from a range of forest, moorland and agricultural soils, Biogeochemistry, 34, 113–132, 1996.

Martin, A., Gayler, V., Steil, B., Klingmüller, K., Jöckel, P., Tost, H., Lelieveld, J., and Pozzer, A.: Evaluation of the coupling of EMACv2. 55 to the land surface and vegetation model JSBACHv4, Geoscientific Model Development, 17, 5705–5732, 2024.

Massart, S., Agusti-Panareda, A., Aben, I., Butz, A., Chevallier, F., Crevoisier, C., Engelen, R., Frankenberg, C., and Hasekamp, O.: Assimilation of atmospheric methane products into the MACC-II system: from SCIAMACHY to TANSO and IASI, Atmospheric Chemistry and Physics, 14, 6139–6158, 2014.

Moldrup, P., Kruse, C., Rolston, D., and Yamaguchi, T.: Modeling diffusion and reaction in soils: III. Predicting gas diffusivity from the Campbell soil-water retention model, Soil science, 161, 366–375, 1996.

Moldrup, P., Chamindu Deepagoda, T., Hamamoto, S., Komatsu, T., Kawamoto, K., Rolston, D. E., and de Jonge, L. W.: Structure-dependent water-induced linear reduction model for predicting gas diffusivity and tortuosity in repacked and intact soil, Vadose Zone Journal, 12, vzj2013–01, 2013.

Murguia-Flores, F., Arndt, S., Ganesan, A. L., Murray-Tortarolo, G., and Hornibrook, E. R.: Soil Methanotrophy Model (MeMo v1. 0): a process-based model to quantify global uptake of atmospheric methane by soil, Geoscientific Model Development, 11, 2009–2032, 2018.

NIES: National Institute for Environmental Studies: GOSAT TANSO-FTS SWIR Level 3 Data Product Format Description, https://data2.gosat.nies.go.jp/GosatDataArchiveService/doc/GU/GOSAT_ProductDescription_31_FTSSWIRL3_BiasCorr_V1.51_en.pdf, 2024.

Nishina, K., Ito, A., Hanasaki, N., and Hayashi, S.: Reconstruction of spatially detailed global map of NH 4+ and NO 3- application in synthetic nitrogen fertilizer, Earth System Science Data, 9, 149–162, Accessed: October 31, 2024, 2017.

NOAA Global Monitoring Laboratory (GML): Atmospheric Methane Data (CH_4) – Global Monthly Means, https://gml.noaa.gov/ccgg/trends/, data freely available from NOAA GML. Contact: Xin Lan (xin.lan@noaa.gov). Please cite appropriately as recommended by NOAA GML. See Dlugokencky et al. (1994), JGR, vol. 99, pp. 17021–17043, for methodology., 2025.

Ostler, A., Sussmann, R., Patra, P. K., Houweling, S., De Bruine, M., Stiller, G. P., Haenel, F. J., Plieninger, J., Bousquet, P., Yin, Y., et al.: Evaluation of column-averaged methane in models and TCCON with a focus on the stratosphere, Atmospheric Measurement Techniques, 9, 4843–4859, 2016.

Ouyang, Z., Jackson, R. B., Saunois, M., Canadell, J. G., Zhao, Y., Morfopoulos, C., Krummel, P. B., Patra, P. K., Peters, G. P., Dennison, F., et al.: The global hydrogen budget, Nature, 648, 616–624, 2025.

Parker, R. J., Webb, A., Boesch, H., Somkuti, P., Barrio Guillo, R., Di Noia, A., Kalaitzi, N., Anand, J. S., Bergamaschi, P., Chevallier, F., et al.: A decade of GOSAT Proxy satellite CH 4 observations, Earth System Science Data, 12, 3383–3412, 2020.

Paulot, F., Paynter, D., Naik, V., Malyshev, S., Menzel, R., and Horowitz, L. W.: Global modeling of hydrogen using GFDL-AM4. 1: Sensitivity of soil removal and radiative forcing, International Journal of Hydrogen Energy, 46, 13 446–13 460, 2021.

Paulot, F., Pétron, G., Crotwell, A. M., and Bertagni, M. B.: Reanalysis of NOAA H 2 observations: implications for the H 2 budget, Atmospheric Chemistry and Physics, 24, 4217–4229, 2024.

https://doi.org/10.5194/egusphere-2026-371
Preprint. Discussion started: 10 February 2026

Pétron, G., Crotwell, A. M., Mund, J., Crotwell, M., Mefford, T., Thoning, K., Hall, B., Kitzis, D., Madronich, M., Moglia, E., et al.: Atmospheric H 2 observations from the NOAA Cooperative Global Air Sampling Network, Atmospheric Measurement Techniques, 17, 4803–4823, 2024.

Phillips, R. L., Whalen, S. C., and Schlesinger, W. H.: Response of soil methanotrophic activity to carbon dioxide enrichment in a North Carolina coniferous forest, Soil Biology and Biochemistry, 33, 793–800, 2001.

Randerson, J. T., van der Werf, G. R., Giglio, L., Collatz, G. J., and Kasibhatla, P. S.: Global Fire Emissions Database, Version 4.1 (GFEDv4), ORNL Distributed Active Archive Center (DAAC) dataset 10.3334/ORNLDAAC/1293 (2017), https://doi.org/10.3334/ORNLDAAC/1293, 2017.

Reick, C. H., Gayler, V., Goll, D., Hagemann, S., Heidkamp, M., and Nabel, J. E. M. S. e. a.: JSBACH 3 - The land component of the MPI Earth System Model: documentation of version 3.2. Hamburg: MPI für Meteorologie, https://doi.org/10.17617/2.3279802, 2021.

Ridgwell, A. J., Marshall, S. J., and Gregson, K.: Consumption of atmospheric methane by soils: A process-based model, Global Biogeochemical Cycles, 13, 59–70, 1999.

Rigler, E. and Zechmeister-Boltenstern, S.: Oxidation of ethylene and methane in forest soils—effect of CO2 and mineral nitrogen, Geoderma, 90, 147–159, 1999.

Rodell, M., Houser, P., Jambor, U., Gottschalck, J., Mitchell, K., Meng, C.-J., Arsenault, K., Cosgrove, B., Radakovich, J., Bosilovich, M., et al.: The global land data assimilation system, Bulletin of the American Meteorological society, 85, 381–394, 2004.

Roeckner, E., Brokopf, R., Esch, M., Giorgetta, M., Hagemann, S., Kornblueh, L., Manzini, E., Schlese, U., and Schulzweida, U.: Sensitivity of simulated climate to horizontal and vertical resolution in the ECHAM5 atmosphere model, Journal of Climate, 19, 3771–3791, 2006.

Sand, M., Skeie, R. B., Sandstad, M., Krishnan, S., Myhre, G., Bryant, H., Derwent, R., Hauglustaine, D., Paulot, F., Prather, M., et al.: A multi-model assessment of the Global Warming Potential of hydrogen, Communications Earth & Environment, 4, 203, 2023.

Saunois, M., Bousquet, P., Poulter, B., Peregon, A., Ciais, P., Canadell, J. G., Dlugokencky, E. J., Etiope, G., Bastviken, D., Houweling, S., et al.: The global methane budget: 2000–2012, Earth System Science Data Discussions, 2016, 1–79, 2016.

Saunois, M., Stavert, A. R., Poulter, B., Bousquet, P., Canadell, J. G., Jackson, R. B., Raymond, P. A., Dlugokencky, E. J., Houweling, S., Patra, P. K., et al.: The global methane budget 2000–2017, Earth System Science Data Discussions, 2019, 1–136, 2019.

Saunois, M., Martinez, A., Poulter, B., Zhang, Z., Raymond, P. A., Regnier, P., Canadell, J. G., Jackson, R. B., Patra, P. K., Bousquet, P., et al.: Global methane budget 2000–2020, Earth System Science Data, 17, 1873–1958, 2025.

Schneck, R., Gayler, V., Nabel, J. E. M. S., Raddatz, T., Reick, C. H., and Schnur, R.: Assessment of JSBACHv4.30 as land component of ICON-ESM-V1 in comparison to its predecessor JSBACHv3.2 of MPI-ESM1.2, Geoscientific Model Development Discussions, 2022, 1–45, https://doi.org/10.5194/gmd-2022-74, 2022.

Schultz, M. G., Diehl, T., Brasseur, G. P., and Zittel, W.: Air pollution and climate-forcing impacts of a global hydrogen economy, Science, 302, 624–627, 2003.

Schultz, M. G., Heil, A., Hoelzemann, J. J., Spessa, A., Thonicke, K., Goldammer, J. G., Held, A. C., Pereira, J. M., and van Het Bolscher, M.: Global wildland fire emissions from 1960 to 2000, Global Biogeochemical Cycles, 22, 2008.

Shangguan, W., Dai, Y., Duan, Q., Liu, B., and Yuan, H.: A global soil data set for earth system modeling, Journal of Advances in Modeling Earth Systems, 6, 249–263, Accessed: October 31, 2024, 2014.

Shushi, P., Zihan, L., Gang, L., and Anping, C.: Global soil methane uptake inferred from global field measurements, https://doi.org/10.5281/zenodo.4019118, 2020.

https://doi.org/10.5194/egusphere-2026-371
Preprint. Discussion started: 10 February 2026

Singh, J., Singh, S., Raghubanshi, A., Singh, S., Kashyap, A., and Reddy, V.: Effect of soil nitrogen, carbon and moisture on methane uptake by dry tropical forest soils, Plant and Soil, 196, 115–121, 1997.

Sitaula, B. K., Hansen, S., Sitaula, J. I. B., and Bakken, L. R.: Methane oxidation potentials and fluxes in agricultural soil: Effects of fertilisation and soil compaction, Biogeochemistry, 48, 323–339, 2000.

Stanevich, I., Jones, D., Strong, K., Keller, M., Henze, D. K., Parker, R. J., Boesch, H., Wunch, D., Notholt, J., Petri, C., et al.: Characterizing model errors in chemical transport modeling of methane: using GOSAT XCH 4 data with weak-constraint four-dimensional variational data assimilation, Atmospheric Chemistry and Physics, 21, 9545–9572, 2021.

Steinkamp, R., Butterbach-Bahl, K., and Papen, H.: Methane oxidation by soils of an N limited and N fertilized spruce forest in the Black Forest, Germany, Soil Biology and Biochemistry, 33, 145–153, 2001.

Surawski, N., Steil, B., Brühl, C., Gromov, S., Klingmüller, K., Martin, A., Pozzer, A., and Lelieveld, J.: Global atmospheric hydrogen chemistry and long-term source-sink budget simulation with the EMAC v2. 55 model, EGUsphere, 2025, 1–29, 2025.

The MESSy Consortium: The Modular Earth Submodel System Version 2.55.2_no-branch_b4754874_H2, https://doi.org/10.5281/zenodo.15211346, 2025.

Tost, H., Jöckel, P., Kerkweg, A., Sander, R., and Lelieveld, J.: A new comprehensive SCAVenging submodel for global atmospheric chemistry modelling, Atmospheric Chemistry and Physics, 6, 565–574, 2006.

Trapani, D., Marocco, P., Gandiglio, M., and Santarelli, M.: Hydrogen leakages across the supply chain: Current estimates and future scenarios, Available at SSRN 5241128, 2025.

Tromp, T. K., Shia, R.-L., Allen, M., Eiler, J. M., and Yung, Y. L.: Potential environmental impact of a hydrogen economy on the stratosphere, science, 300, 1740–1742, 2003.

Van den Pol-van Dasselaar, A., Van Beusichem, M., and Oenema, O.: Effects of soil moisture content and temperature on methane uptake by grasslands on sandy soils, Plant and Soil, 204, 213–222, 1998.

Wang, Y., Xue, M., Zheng, X., Ji, B., Du, R., and Wang, Y.: Effects of environmental factors on N2O emission from and CH4 uptake by the typical grasslands in the Inner Mongolia, Chemosphere, 58, 205–215, 2005.

Whalen, S.: Influence of N and non-N salts on atmospheric methane oxidation by upland boreal forest and tundra soils, Biology and Fertility of Soils, 31, 279–287, 2000.

Yashiro, H., Sudo, K., Yonemura, S., and Takigawa, M.: The impact of soil uptake on the global distribution of molecular hydrogen: chemical transport model simulation, Atmospheric Chemistry and Physics, 11, 6701–6719, 2011.

Yonemura, S., Yokozawa, M., Kawashima, S., and Tsuruta, H.: Model analysis of the influence of gas diffusivity in soil on CO and H2 uptake, Tellus B: Chemical and Physical Meteorology, 52, 919–933, 2000.

Yoshida, Y., Kikuchi, N., Morino, I., Uchino, O., Oshchepkov, S., Bril, A., Saeki, T., Schutgens, N., Toon, G., Wunch, D., et al.: Improvement of the retrieval algorithm for GOSAT SWIR XCO 2 and XCH 4 and their validation using TCCON data, Atmospheric Measurement Techniques, 6, 1533–1547, 2013.

Zhuang, Q., Chen, M., Xu, K., Tang, J., Saikawa, E., Lu, Y., Melillo, J. M., Prinn, R. G., and McGuire, A. D.: Response of global soil consumption of atmospheric methane to changes in atmospheric climate and nitrogen deposition, Global Biogeochemical Cycles, 27, 650–663, 2013.

Zimmermann, P. H., Brenninkmeijer, C. A., Pozzer, A., Jöckel, P., Winterstein, F., Zahn, A., Houweling, S., and Lelieveld, J.: Model simulations of atmospheric methane (1997–2016) and their evaluation using NOAA and AGAGE surface and IAGOS-CARIBIC aircraft observations, Atmospheric Chemistry and Physics, 20, 5787–5809, 2020.